Available online at www.sciencedirect.com
ScienceDirect
Engineering Fracture Mechanics 75 (2008) 2062–2086
Engineering Fracture Mechanics
www.elsevier.com/locate/engfracmech

Stochastic multiscale models for fracture analysis of functionally graded materials

Arindam Chakraborty, Sharif Rahman *

Department of Mechanical and Industrial Engineering, College of Engineering, The University of Iowa, Iowa City, IA 52242, United States

Received 22 June 2007; received in revised form 12 October 2007; accepted 18 October 2007
Available online 1 November 2007

Abstract

This article presents three multiscale models, including sequential, invasive, and concurrent models, for fracture analysis of a crack in a two-phase, functionally graded composite. The models involve stochastic description of the particle volume fractions, particle locations, and constituent material properties; a two-scale algorithm including microscale and macroscale analyses for determining crack-driving forces; and two stochastic methods for fracture reliability analysis. The particle volume fractions, defined by a generic inhomogeneous random field, are related to the intensity function of an inhomogeneous Poisson field, which describes the statistically inhomogeneous microstructure of a functionally graded composite. Two stochastic methods, the dimensional decomposition method and direct Monte Carlo simulation, have been employed for obtaining the probabilistic characteristics of crack-driving forces and reliability analysis. Numerical results indicate that the sequential and invasive multiscale models are the most computationally inexpensive models available, but they may not produce acceptable probabilistic characteristics of stress-intensity factors or accurate probability of fracture initiation. The concurrent multiscale model is sufficiently accurate, gives probabilistic solutions very close to those generated from the microscale model, and can reduce the computational effort of the latter model by more than a factor of two. In addition, the concurrent multiscale model predicts crack trajectory as accurately as the microscale model.

Keywords: Sequential multiscale; Invasive multiscale; Concurrent multiscale; Microscale; Random field; Volume fraction; Random microstructure; Fracture reliability

1. Introduction

A functionally graded material (FGM) is an engineered composite medium in which the composition of constituent material phases and hence the microstructure varies spatially to produce a desired functional performance. An FGM derived from an optimized compositional variation and microstructure rather than traditional designs can lead to improved fatigue durability and thermal performance of a mechanical system [1]. However, the extent to which an FGM can be tailored to produce target mechanical performance depends on a sound theoretical understanding of the fracture behavior and reliability of FGMs.

* Corresponding author. Tel.: +1 319 335 5679; fax: +1 319 335 5669.
E-mail address: rahman@engineering.uiowa.edu (S. Rahman).

0013-7944/$ - see front matter © 2007 Elsevier Ltd. All rights reserved.
doi:10.1016/j.engfracmech.2007.10.013

During the last few decades, various theoretical [2–4] and computational [5–8] studies have been conducted on fracture behavior of FGMs. A significant part of these studies involves developing new or refined methods for accurately calculating stress-intensity factors (SIFs) in isotropic [5–7] or orthotropic [8] media. It is typically assumed that the effective material properties of FGM, required for calculating crack-driving forces, are smoothly varying and can be calculated from various rules of mixture or classical micromechanical homogenization [9,10]. The application of the resultant effective properties to study FGM fracture processes, while generally useful for characterizing a global response, poses at least two problems. First, FGM is a multiphase material with distinct properties of individual material phases. A crack in a two-phase FGM may have significantly different energetics, depending on whether the crack tip is located at phase 1 or phase 2 of the FGM. Therefore, assuming homogenized properties, which is an approximation at best, may provide inaccurate or inadequate measures of crack-driving forces. Due to sharp discontinuities in the material properties at the microstructural length scale, a multiscale analysis is desirable and may be required to determine if, indeed, effective properties can be employed for describing behavior near a crack tip [11]. Second, an FGM microstructure is inherently stochastic and can, in fact, be viewed as a statistically inhomogeneous random field [12,13], which describes randomness in the density, location, size, and shape characteristics of embedded particles in a matrix. Furthermore, the phase volume fractions and constituent material properties may also be stochastic. Clearly, an FGM fracture analysis is a stochastic-mechanics problem, which, therefore, calls for examining the adequacy of FGM effective properties based on the probabilistic characteristics of relevant crack-driving forces. Unfortunately, research in stochastic modeling of FGMs has not been widespread and is only now gaining attention [14,15]. For example, the authors have recently developed a stochastic micromechanical model for obtaining probabilistic descriptors of effective FGM properties, given the statistical characteristics of constituents and their respective volume fractions [15]. While such works are encouraging and constitute a step in the right direction, more general probabilistic models are required that are capable of uncovering multiscale fracture behavior of FGMs. Indeed, stochastic multiscale fracture is a rich and relatively unexplored subject area, and further research is required to provide a clear picture of how and/or if effective properties can be exploited to evaluate crack-driving forces and reliability of FGMs.

This paper presents three stochastic multiscale models for fracture analysis of a crack in a two-phase, functionally graded, particle–matrix composite. The models involve: (1) stochastic description of the particle volume fractions, particle locations, and constituent material properties, (2) a two-scale algorithm including microscale and macroscale analyses for determining crack-driving forces, and (3) two stochastic methods for uncertainty propagation and fracture reliability analysis. Section 2 describes a generic fracture problem, defines random input parameters, and discusses crack-driving forces and fracture reliability. Section 3 presents three distinct multiscale models, including sequential, invasive, and concurrent algorithms, for calculating various response characteristics of interest. A full microscale model is also presented to evaluate the multiscale models. Section 4 describes the dimensional decomposition and direct Monte Carlo methods for calculating statistical moments and probability densities of crack-driving forces, leading to the probability of fracture initiation. A numerical example employing various multiscale and microscale models is presented in Section 5. Finally, Section 6 provides conclusions from this work.

2. Stochastic fracture problem

2.1. Problem statement

Consider a two-phase, functionally graded, heterogeneous solid with a rectilinear crack and domain $\mathscr{D} \subset \mathbb{R}^2$ and a schematic illustration of its microstructure, as shown in Fig. 1. The microstructure includes two distinct material phases, phase p (green or dark)[1] and phase m (white or light), denoting particle and matrix constituents, respectively. Both constituents represent isotropic and linear-elastic materials, and the elasticity tensors of the particle and matrix, denoted by $\boldsymbol{C}^{(p)}$ and $\boldsymbol{C}^{(m)}$, respectively, are

[1] For interpretation of color in Fig. 1, the reader is referred to the web version of this article.

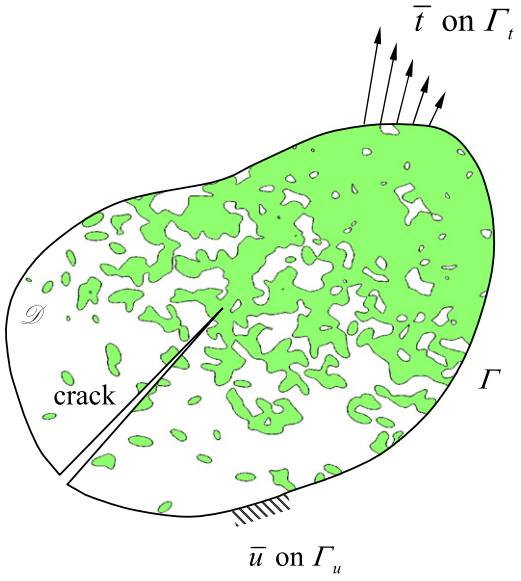

Fig. 1. A crack in a two-phase, particle–matrix, functionally graded composite.

$$\boldsymbol{C}^{(i)} := \frac{v_i E_i}{(1+v_i)(1-2v_i)}\mathbf{1}\otimes\mathbf{1} + \frac{E_i}{(1+v_i)}\boldsymbol{I}; \quad i = p, m, \tag{1}$$

where the symbol $\otimes$ denotes the tensor product; E_i and v_i are the elastic modulus and Poisson's ratio, respectively, of phase i; and $\mathbf{1}$ and $\boldsymbol{I}$ are second- and fourth-rank identity tensors, respectively. The superscripts or subscripts $i = p$ and $i = m$ refer to particle and matrix, respectively. At a spatial point $\boldsymbol{x} \in \mathscr{D}$ in the macroscopic length scale, let $\phi_p(\boldsymbol{x})$ and $\phi_m(\boldsymbol{x})$ denote the volume fractions of particle and matrix, respectively. Each volume fraction is bounded between 0 and 1 and satisfies the constraint $\phi_p(\boldsymbol{x}) + \phi_m(\boldsymbol{x}) = 1$. The crack faces are traction-free, and there is perfect bonding between matrix and particles. In addition, no porosities are included in the matrix or particle phases.

Consider a linear-elastic solid with small displacements and strains. The equilibrium equation and boundary conditions for the quasi-static problem are

$$\nabla\cdot\boldsymbol{\sigma} + \boldsymbol{b} = \mathbf{0} \text{ in } \mathscr{D} \quad \text{and} \tag{2}$$

$$\begin{matrix}\boldsymbol{\sigma}\cdot\boldsymbol{n} = \bar{\boldsymbol{t}} \text{ on } \Gamma_t \text{ (natural boundary conditions)} \\ \boldsymbol{u} = \bar{\boldsymbol{u}} \text{ on } \Gamma_u \text{ (essential boundary conditions)}\end{matrix}, \tag{3}$$

respectively, where $\boldsymbol{u} : \mathscr{D} \to \mathbb{R}^2$ is the displacement vector; $\boldsymbol{\sigma} = \boldsymbol{C}(\boldsymbol{x}) : \boldsymbol{\epsilon}$ is the Cauchy stress tensor with $\boldsymbol{C}(\boldsymbol{x})$ and $\boldsymbol{\epsilon} := (1/2)(\nabla + \nabla^{\mathrm{T}})\boldsymbol{u}$ denoting the spatially variant elasticity tensor and strain tensor, respectively; $\boldsymbol{n}$ is a unit outward normal to the boundary Γ of the solid; Γ_t and Γ_u are two disjoint portions of the boundary Γ, where the traction vector $\bar{\boldsymbol{t}}$ and displacement $\bar{\boldsymbol{u}}$ are prescribed; $\nabla^{\mathrm{T}} := \{\partial/\partial x_1, \partial/\partial x_2\}$ is the vector of gradient operators; and symbols "." and ":" denote dot product and tensor contraction, respectively.

The variational or weak form of Eqs. (2) and (3) is

$$\int_{\mathscr{D}} (\boldsymbol{C}(\boldsymbol{x}) : \boldsymbol{\epsilon}) : \delta\boldsymbol{\epsilon}\,\mathrm{d}\mathscr{D} - \int_{\mathscr{D}} \boldsymbol{b}\cdot\delta\boldsymbol{u}\,\mathrm{d}\mathscr{D} - \int_{\Omega} \bar{\boldsymbol{t}}\cdot\delta\boldsymbol{u}\,\mathrm{d}\Gamma - \sum_{x_K\in\Gamma_u} \boldsymbol{f}(\boldsymbol{x}_K)\cdot\delta\boldsymbol{u}(\boldsymbol{x}_K) - \sum_{x_K\in\Gamma_u} \delta\boldsymbol{f}(\boldsymbol{x}_K)\cdot[\boldsymbol{u}(\boldsymbol{x}_K) - \bar{\boldsymbol{u}}(\boldsymbol{x}_K)] = 0, \tag{4}$$

where $\boldsymbol{f}^{\mathrm{T}}(\boldsymbol{x}_K)$ is the vector of reaction forces at a constrained node K on Γ_u, and δ denotes the variation operator. The discretization of the weak form, Eq. (4), depends on how the elasticity tensor $\boldsymbol{C}(\boldsymbol{x})$ is defined, i.e., how the elastic properties of constituent material phases and their gradation characteristics are described. In the following section, various multiscale and uniscale models are presented to approximate $\boldsymbol{C}(\boldsymbol{x})$. Nonetheless, a

numerical method, e.g., the finite-element method (FEM), is generally required to solve the discretized weak form, providing various response fields of interest.

2.2. Statistical models of random input

Uncertainties in FGM fracture can come from a variety of sources – for instance, the FGM microstructure, constituent material properties, boundary conditions, crack geometry, and structural geometry. Microstructural uncertainty includes randomness in particle volume fractions, spatial arrangements of particles, and size, shape, and orientation properties of particles. In this work, however, the sources of uncertainties are limited to particle volume fractions, particle locations, and constituent material properties and are described as follows.

2.2.1. Particle volume fraction

Let $(\Omega, \mathscr{F}, P)$ be a probability space, where Ω is the sample space, $\mathscr{F}$ is the σ-algebra of subsets of Ω, and P is the probability measure. Defined on the probability triple $(\Omega, \mathscr{F}, P)$ and endowed with the expectation operator $\mathbb{E}$, the particle volume fraction $\phi_p(\boldsymbol{x})$ can be modeled as an inhomogeneous (non-stationary), non-Gaussian, random field, which has mean $\mu_p(\boldsymbol{x})$ and standard deviation $\sigma_p(\boldsymbol{x})$ [15]. The standardized particle volume fraction

$$\tilde{\phi}_p(\boldsymbol{x}) := \frac{\phi_p(\boldsymbol{x}) - \mu_p(\boldsymbol{x})}{\sigma_p(\boldsymbol{x})}, \tag{5}$$

which has zero mean and unit variance, is at least a weakly homogeneous (stationary) random field with a prescribed covariance function $\Gamma_{\tilde{\phi}_p}(\boldsymbol{s}) := \mathbb{E}[\tilde{\phi}_p(\boldsymbol{x})\tilde{\phi}_p(\boldsymbol{x}+\boldsymbol{s})]$ and a marginal cumulative distribution function $F_p(\tilde{\phi}_p)$ such that $0 \leqslant \phi_p(\boldsymbol{x}) \leqslant 1$ with probability one. If the covariance function $\Gamma_{\tilde{\phi}_p}(\boldsymbol{s})$ is appropriately bounded, the standardized phase volume fraction can be viewed as a translation random field $\tilde{\phi}_p(\boldsymbol{x}) = G_p[\alpha_p(\boldsymbol{x})] := F_p^{-1}[\Phi(\alpha_p(\boldsymbol{x}))]$, where G_p is a mapping of the Gaussian field on a non-Gaussian field, $\alpha_p(\boldsymbol{x})$ is the Gaussian image field and $\Phi(\cdot)$ is the distribution function of a standard Gaussian random variable. Subsequently, the Karhunen–Loève approximation of the image field leads to [15]

$$\tilde{\phi}_p(\boldsymbol{x}) \cong G_p\left[\sum_{k=1}^{M} Z_{p,k}\sqrt{\lambda_{p,k}}\Psi_{p,k}(\boldsymbol{x})\right], \tag{6}$$

where $\lambda_{p,k}$ and $\Psi_{p,k}(\boldsymbol{x})$ denote the kth eigenvalue and kth eigenfunction, respectively, of the covariance function of $\alpha_p(\boldsymbol{x})$, and $Z_{p,k}$ is an independent copy of a standard Gaussian random variable. According to Eq. (6), the Karhunen–Loève approximation yields a parametric representation of the standardized phase volume fraction $\tilde{\phi}_p(\boldsymbol{x})$ and, hence, of $\phi_p(\boldsymbol{x})$ with M Gaussian variables. The random field description of $\phi_p(\boldsymbol{x})$ allows a volume fraction to have random fluctuation at a point $\boldsymbol{x}$ in the macroscopic length scale. Further details are available in the authors' previous work [15].

2.2.2. Particle location

The random microstructure entailing particle locations can be described using the well-known Poisson random field. However, since the FGM microstructure varies spatially, the Poisson field must be inhomogeneous. Therefore, consider an inhomogeneous Poisson field $\mathscr{N}(\mathscr{D}')$ with an intensity measure $\mu_{\mathscr{D}'} := \int_{\mathscr{D}'} \lambda(\boldsymbol{x})\,\mathrm{d}\boldsymbol{x}$, where $\lambda(\boldsymbol{x}) \geqslant 0$ is a spatially variant intensity function and $\mathscr{D}' \in \mathscr{B}(\mathbb{R}^2)$ is a bounded Borel set. The Poisson point field has the following properties: (1) the number $\mathscr{N}(\mathscr{D}')$ of points in a bounded subset $\mathscr{D}'$ has the Poisson distribution with intensity measure $\mu_{\mathscr{D}'}$; and (2) random variables $\mathscr{N}(\mathscr{D}'_1), \ldots, \mathscr{N}(\mathscr{D}'_K)$ for any integer $K \geqslant 2$ and disjoint sets $\mathscr{D}'_1, \ldots, \mathscr{D}'_K$ are statistically independent. The Poisson field $\mathscr{N}(\mathscr{D}')$ gives the number of points in $\mathscr{D}'$ and is characterized by the probability

$$P[\mathscr{N}(\mathscr{D}') = k] = \frac{\left(\int_{\mathscr{D}'} \lambda(\boldsymbol{x})\mathrm{d}\boldsymbol{x}\right)^k}{k!} \exp\left(-\int_{\mathscr{D}'} \lambda(\boldsymbol{x})\,\mathrm{d}\boldsymbol{x}\right); \quad k = 0, 1, 2, \ldots \tag{7}$$

that k Poisson points exist in $\mathscr{D}'$. The mean $\mathbb{E}[\mathscr{N}(\mathscr{D}')]$ and variance $\mathrm{Var}[\mathscr{N}(\mathscr{D}')]$ of $\mathscr{N}(\mathscr{D}')$ are both equal to $\mu_{\mathscr{D}'} := \int_{\mathscr{D}'} \lambda(\boldsymbol{x})\mathrm{d}\boldsymbol{x}$. Both $\mathscr{D}$ and $\mathscr{D}'$ are bounded subsets of $\mathbb{R}^2$ such that points of $\mathscr{N}$ falling in the set difference

$\mathbb{R}^2 \setminus \mathscr{D}'$ do not contribute to particles in $\mathscr{D}$. The intensity function is related to the particle volume fraction of the FGM. If the particle volume fraction is a random field, so is the intensity function. An inhomogeneous Poisson field with a random intensity function is known as the doubly stochastic Poisson field. For special cases of particle geometry, explicit forms of the relationship can be derived. For instance, an FGM with fully penetrable circular or spherical particles that have the same deterministic size, as assumed in this work, and a deterministic particle volume fraction $\varphi_p(\boldsymbol{x})$ has the intensity function [16]

$$\lambda(\boldsymbol{x}) \cong \frac{1}{A_p} \ln\left[\frac{1}{1-\varphi_p(\boldsymbol{x})}\right]; \quad \boldsymbol{x} \in \mathscr{D}, \tag{8}$$

where A_p is the common cross-sectional area of the particles. When $\phi_p(\boldsymbol{x})$ is a random field, as treated in this work, $\varphi_p(\boldsymbol{x})$ can be viewed as a sample function of $\phi_p(\boldsymbol{x})$. For more complex microstructures comprising random particle geometry, no such closed-form relationships exist, but they can be formulated algorithmically [13].

Once the intensity function has been determined, samples of synthetic microstructures of two-phase FGMs can be generated based on the following algorithm:

- *Step 1:* Define bounded subsets $\mathscr{D}$ and $\mathscr{D}'$ of $\mathbb{R}^2$. The bounded subset $\mathscr{D}'$ must be such that points of $\mathscr{N}$ falling in $\mathbb{R}^2 \setminus \mathscr{D}'$ do not contribute to particles in $\mathscr{D}$.
- *Step 2:* Generate a sample $\varphi_p(\boldsymbol{x})$ of the random particle volume fraction $\phi_p(\boldsymbol{x})$ using Eqs. (5) and (6). Calculate the corresponding sample $\lambda(\boldsymbol{x})$ of the random intensity function from Eq. (8).
- *Step 3:* Generate a sample k^* of the homogeneous Poisson random variable $N^*(\mathscr{D}')$, which has a constant intensity $\lambda^* = \max_{\boldsymbol{x}\in\mathbb{R}^2}\lambda(\boldsymbol{x})$, where $\lambda(\boldsymbol{x})$ is a bounded intensity function in $\mathscr{D}'$.
- *Step 4:* Generate k^* independent samples of uniformly distributed points $(u_{i,1}, u_{i,2})$ in $\mathscr{D}'$. Denote these points by $\boldsymbol{x}_i$, $i = 1, \ldots, k^*$.
- *Step 5:* Perform thinning of the point set obtained in Step 4. In so doing, each point $\boldsymbol{x}_i$, independently of the other, is kept with probability $\lambda(\boldsymbol{x}_i)/\lambda^*$, which is equivalent to discarding the point with probability $1 - \lambda(\boldsymbol{x}_i)/\lambda^*$. The resulting point pattern with the size $k \leqslant k^*$ follows the inhomogeneous Poisson field $\mathscr{N}(\mathscr{D}')$ with the intensity function $\lambda(\boldsymbol{x})$. Let these points be denoted by $\boldsymbol{\Gamma}_i$, $i = 1, \ldots, k$.
- *Step 6:* Place particles with their centroids coincident with the points $\boldsymbol{\Gamma}_i$, $i = 1, \ldots, k$. The resultant subsets of particle and matrix regions in $\mathscr{D}$ produce a sample of a two-phase statistically inhomogeneous microstructure.

Independent samples of random microstructure are delivered by repeated application of the above algorithm.

2.2.3. Constituent material properties

In addition to a spatially variant random volume fraction of particles leading to a random microstructure, the constituent properties of material phases can be stochastic. Defined on the same probability space $(\Omega, \mathscr{F}, P)$, let E_p and ν_p denote the elastic modulus and Poisson's ratio, respectively, of the particle and E_m and ν_m denote the elastic modulus and Poisson's ratio, respectively, of the matrix. Therefore, the random vector $\{E_p, E_m, \nu_p, \nu_m\}^{\mathrm{T}} \in \mathbb{R}^4$ describes the stochastic elastic properties of both constituents. Unlike volume fractions, however, the constituent properties are spatially invariant in the macroscopic length scale.

In summary, the random variables may include: (1) M random variables $\{Z_{p,1}, \ldots, Z_{p,M}\}$ due to the discretization of the random field $\phi_p(\boldsymbol{x})$; (2) a Poisson random variable $\mathscr{N}$ and resulting $2\mathscr{N}$ random variables $\{(U_{i,1}, U_{i,2})\}; i = 1, \ldots, \mathscr{N}$ representing coordinates of the centroids of the particles in $\mathscr{D}'$; and (3) four random constituent properties $\{E_p, E_m, \nu_p, \nu_m\}$. Depending on the multiscale model employed, some or all of these random variables can be accounted for in a stochastic analysis. Nevertheless, the maximum value of the total number of random variables N is $M + 2\mathscr{N} + 5$. In other words, an input random vector $\boldsymbol{R} = \{Z_{p,1}, \ldots, Z_{p,M}, \mathscr{N}, (U_{1,1}, U_{1,2}), \ldots, (U_{\mathscr{N},1}, U_{\mathscr{N},2}), E_p, E_m, \nu_p, \nu_m\}^{\mathrm{T}} \in \mathbb{R}^N$ characterizes uncertainties from all sources in an FGM and is completely described by its known joint probability density function (PDF) $f_{\boldsymbol{R}}(\boldsymbol{r})$, where $\boldsymbol{r}$ is a realization of $\boldsymbol{R}$.

2.3. Crack-driving forces and reliability

2.3.1. Crack-driving forces

A major objective of stochastic fracture-mechanics analysis is to find probabilistic characteristics of crack-driving forces, such as SIFs $K_{\mathrm{I}}(\boldsymbol{R})$ and $K_{\mathrm{II}}(\boldsymbol{R})$ for modes I and II, respectively, the J-integral, and other fracture integrals, due to uncertain input $\boldsymbol{R}$. For a given input, the standard FEM can be employed to solve the discretized weak form (Eq. (4)), leading to the calculation of SIFs and other crack-driving forces. Let $y(\boldsymbol{R})$ describe a generic crack-driving force or a relevant performance function involving crack-driving forces for a given fracture problem of interest. In general, the multivariate function $y : \mathbb{R}^N \to \mathbb{R}$ is implicit, is not analytically available, and can only be viewed as a high-dimensional input–output mapping, where the evaluation of the output function y for a given input $\boldsymbol{r}$ requires expensive finite-element analysis. Therefore, methods employed in stochastic analysis must be capable of generating accurate probabilistic characteristics of $y(\boldsymbol{R})$ with an acceptably small number of output function evaluations.

2.3.2. Reliability

Suppose that failure is defined when the crack propagation is initiated at a crack tip, i.e., when $K_{\mathrm{eff}}(\boldsymbol{R}) = h(K_{\mathrm{I}}(\boldsymbol{R}),\ K_{\mathrm{II}}(\boldsymbol{R})) > K_{\mathrm{Ic}}$, where K_{eff} is an effective SIF with h depending on a selected mixed-mode theory, and K_{Ic} is a relevant mode-I fracture toughness of the material measured in terms of SIF. This requirement cannot be satisfied with certainty, since K_{I} and K_{II} are both dependent on $\boldsymbol{R}$, which is random, and K_{Ic} itself may be a random variable or field. Hence, the performance of a cracked FGM should be evaluated by the reliability or its complement, the probability of failure P_{F}, defined as the multifold integral

$$P_{\mathrm{F}}(K_{\mathrm{Ic}}) := P[y(\boldsymbol{R}) < 0] := \int_{\mathbb{R}^N} \mathbb{I}_y(\boldsymbol{r}) f_{\boldsymbol{R}}(\boldsymbol{r}) \mathrm{d}\boldsymbol{r}, \tag{9}$$

where

$$y(\boldsymbol{R}) = K_{\mathrm{Ic}} - h(K_{\mathrm{I}}(\boldsymbol{R}), K_{\mathrm{II}}(\boldsymbol{R})) \tag{10}$$

is a multivariate performance function that depends on the random input $\boldsymbol{R}$ and

$$\mathbb{I}_y(\boldsymbol{r}) = \begin{cases} 1, & \text{if } y(\boldsymbol{r}) < 0 \\ 0, & \text{if } y(\boldsymbol{r}) > 0 \end{cases} \tag{11}$$

is an indicator function. For example, if the maximum circumferential stress theory is invoked to describe a mixed-mode fracture initiation [17], the associated performance function is

$$y(\boldsymbol{R}) = K_{\mathrm{Ic}} - \left[K_{\mathrm{I}}(\boldsymbol{R}) \cos^2 \frac{\Theta(\boldsymbol{R})}{2} - \frac{3}{2} K_{\mathrm{II}}(\boldsymbol{R}) \sin \Theta(\boldsymbol{R}) \right] \cos \frac{\Theta(\boldsymbol{R})}{2} \tag{12}$$

with

$$\Theta(\boldsymbol{R}) = \begin{cases} 2 \tan^{-1} \left(\frac{K_{\mathrm{I}}(\boldsymbol{R})}{4 K_{\mathrm{II}}(\boldsymbol{R})} - \frac{1}{4} \sqrt{\frac{K_{\mathrm{I}}^2(\boldsymbol{R})}{K_{\mathrm{II}}^2(\boldsymbol{R})} + 8} \right), & \text{if } K_{\mathrm{II}}(\boldsymbol{R}) > 0 \\ 2 \tan^{-1} \left(\frac{K_{\mathrm{I}}(\boldsymbol{R})}{4 K_{\mathrm{II}}(\boldsymbol{R})} + \frac{1}{4} \sqrt{\frac{K_{\mathrm{I}}^2(\boldsymbol{R})}{K_{\mathrm{II}}^2(\boldsymbol{R})} + 8} \right), & \text{if } K_{\mathrm{II}}(\boldsymbol{R}) < 0 \end{cases} \tag{13}$$

denoting the angle of crack propagation. Any other mixed-mode theory can be easily incorporated in the probabilistic framework developed, leading to similar performance functions.

The evaluation of the multidimensional integral in Eq. (9), either analytically or numerically, is not possible because the total number of random variables N is large, $f_{\boldsymbol{R}}(\boldsymbol{r})$ is generally non-Gaussian, and $y(\boldsymbol{r})$ is a highly nonlinear function of $\boldsymbol{r}$. In this work, the dimensional decomposition method and direct Monte Carlo simulation were employed for calculating the probabilistic characteristics of crack-driving forces and the probability of fracture initiation. Further explanation of these stochastic methods is given in Section 4.

3. Multiscale and microscale analyses

The FGM microstructure schematically illustrated in Fig. 1 contains discontinuities in material properties at the interfaces between the matrix and particles. However, it is unclear how such discontinuities will affect the calculation of a SIF. In addition, a mathematically sharp crack tip, which has no geometric dimensions, is located in either the matrix or the particle phase. Employing an effective elastic modulus, commonly used for deriving the energy release rate of a cracked solid, may yield inadequate estimates of the resultant SIFs, particularly if there exists a significant mismatch between the matrix and particle properties. Furthermore, the calculation of effective properties requires a representative volume element, which loses its meaning for a region close to the crack tip due to high stress and strain gradients. However, far away from the crack tip, where the effect of the crack-tip singularity dies off rapidly, individual constituent material properties may not be needed, and an appropriately derived effective material property should suffice.

From the above discussion, there exist two major approaches with respect to defining the material property for fracture analysis of an FGM cracked structure. One approach involves stress analysis using effective material property in the domain of the solid. This approach is referred to as macroscale analysis. The other approach, referred to as microscale analysis, entails stress analysis that is solely based on the exact material property information derived from the knowledge of explicit particle location and geometry or volume fraction. A multiscale analysis is a hybrid approach, where both macroscale and microscale analysis are employed. In this work, one microscale and three multiscale models were examined.

3.1. Multiscale analyses

The multiscale analysis can be conducted in several ways, depending on how the information derived from the lower scale (microscale) transfers to or interacts with the analysis in the higher scale (macroscale). However, the mechanics and stochastics involved vary depending on the multiscale model selected and are described in the following subsections.

All multiscale models presented here require continuously varying effective properties, defined either completely or partially in the domain of the solid. Typically, a micromechanical analysis is performed to predict response fields of interest in the microscale, followed by a homogenization to produce the continuously varying effective properties. Let $\overline{\boldsymbol{C}}(\boldsymbol{x})$ denote the continuously varying effective elasticity tensor of the FGM at a point $\boldsymbol{x} \in \mathscr{D}$, expressed by

$$\overline{\boldsymbol{C}}(\boldsymbol{x}) = \frac{\bar{\nu}(\boldsymbol{x})\overline{E}(\boldsymbol{x})}{[1+\bar{\nu}(\boldsymbol{x})][1-2\bar{\nu}(\boldsymbol{x})]}\mathbf{1}\otimes\mathbf{1} + \frac{\overline{E}(\boldsymbol{x})}{[1+\bar{\nu}(\boldsymbol{x})]}\boldsymbol{I}, \tag{14}$$

where the effective elastic modulus $\overline{E}(\boldsymbol{x})$ and effective Poisson's ratio $\bar{\nu}(\boldsymbol{x})$ both depend on $\boldsymbol{x} \in \mathscr{D}$. Using classical micromechanics-for instance, the self-consistent model, the Mori–Tanaka model, the mean-field theory, and others [9,10] -the effective elasticity tensor $\overline{\boldsymbol{C}}(\boldsymbol{x})$ can be readily calculated.

3.1.1. Sequential multiscale model

The sequential or hierarchical multiscale model adopted in the present work includes a three-step serial process. First, the effective tensor $\overline{\boldsymbol{C}}(\boldsymbol{x})$ is calculated using micromechanics based homogenization. Second, a macromechanical stress analysis based on the effective elasticity tensor is conducted to generate the field solutions. In this step, the weak form, described by Eq. (4), is discretized using

$$\boldsymbol{C}(\boldsymbol{x}) \cong \overline{\boldsymbol{C}}(\boldsymbol{x}), \quad \boldsymbol{x} \in \mathscr{D} \tag{15}$$

and then solved by the FEM or other numerical methods, leading to stress, strain, and displacement fields in the macroscopic length scale.

Third, a macromechanical fracture-mechanics analysis using an interaction integral for *inhomogeneous* materials yields the mixed-mode SIFs [5]. Let $\widetilde{M}^{(1,2)}$ denotes the interaction integral for a crack tip in an inhomogeneous material where state 1 represents the *actual* state associated with the given boundary conditions (i.e., the given problem); state 2 represents a known *auxiliary* state, which can be either mode-I or mode-II near-tip displacement and stress fields. The individual SIFs for the actual state can be obtained by judiciously

choosing the auxiliary state (state 2). For example, if state 2 is chosen to be state I (state II), i.e., the mode-I (mode-II) near-tip displacement and stress fields are chosen as the auxiliary state,

$$K_i \cong \frac{1}{2}\widetilde{M}^{(1,i)}\overline{E}^*_{\text{tip}}; \quad i = \text{I, II}, \tag{16}$$

where $\overline{E}^*_{\text{tip}}$, equal to $\overline{E}(\boldsymbol{x}_{\text{tip}})$ for the plane stress and $\overline{E}(\boldsymbol{x}_{\text{tip}})/[1-\bar{\nu}^2(\boldsymbol{x}_{\text{tip}})]$. for the plane strain conditions, is the effective generalized modulus of the FGM at the crack tip $\boldsymbol{x}_{\text{tip}}$, and $\widetilde{M}^{(1,\text{I})}$ and $\widetilde{M}^{(1,\text{II})}$ are two interaction integrals for modes I and II, respectively. Further details about the interaction integral method for inhomogeneous materials is available elsewhere [5].

Dolbow and Nadeau [11] proposed a slight variant of the sequential model, referred to as the weighted sequential model in this paper. In both the original and weighted sequential models, the first two steps and the part of the last step that calculates the interaction integrals $\widetilde{M}^{(1,\text{I})}$ and $\widetilde{M}^{(1,\text{II})}$ are identical. However, in the last step of the weighted sequential model, the mixed-mode SIFs are calculated from the interaction integrals with $\overline{E}^*_{\text{tip}}$ replaced by a weighted sum of E^*_p and E^*_m, yielding

$$K_i \cong \frac{1}{2}\widetilde{M}^{(1,i)}\Big[\phi_p(\boldsymbol{x}_{\text{tip}})E^*_p + \big\{1-\phi_p(\boldsymbol{x}_{\text{tip}})\big\}E^*_m\Big]; \quad i = \text{I, II}, \tag{17}$$

where $E^*_j = E_j$ for the plane stress, $E^*_j = E_j/[1-\nu_j^2]$. for the plane strain conditions, and $j = p, m$. The weighted sum that appears inside the square parenthesis of Eq. (17) represents the expected (mean) value of the generalized modulus at the crack tip, where the volume fractions of material phases act as weights. Therefore, both the original and weighted sequential models involve an averaged elastic modulus, although their results may vary depending on which micromechanical model is employed to determine $\overline{E}^*_{\text{tip}}$. Nonetheless, the explicit effect of particles in the crack-tip region and their stochastics discussed in Section 2.2.2 cannot be accounted for in either version of the sequential model.

For stochastic analysis, the sequential and weighted sequential multiscale models account for statistical uncertainties only in the particle volume fraction $\phi_p(\boldsymbol{x})$ and constituent material properties $\{E_p, E_m, \nu_p, \nu_m\}^{\text{T}}$. Therefore, the input vector $\boldsymbol{R} = \{Z_{p,1}, \ldots, Z_{p,M}, E_p, E_m, \nu_p, \nu_m\}^{\text{T}} \in \mathbb{R}^N$, where the total number of random variables $N = M + 4$.

3.1.2. Invasive multiscale model

The invasive multiscale model also involves a three-step serial process: (1) a micromechanical analysis to predict response fields of interest in the microscale, followed by a homogenization to produce smoothly varying effective properties in the macroscale; (2) a micro–macromechanical stress analysis based on locally homogeneous material properties to generate the field solutions; and (3) a macromechanical fracture analysis based on locally homogeneous material properties to calculate the mixed-mode SIFs.

In the invasive multiscale model, the effective elasticity tensor is also calculated from a micromechanical homogenization, as in the sequential and weighted sequential models. However, the weak form, Eq. (4), is discretized and then solved using

$$\boldsymbol{C}(\boldsymbol{x}) \cong \begin{cases} \boldsymbol{C}^{(p)}, & \text{if } \boldsymbol{x} \in \mathscr{D}_\epsilon \text{ and } \boldsymbol{x}_{\text{tip}} \in \mathscr{D}_p \\ \boldsymbol{C}^{(m)}, & \text{if } \boldsymbol{x} \in \mathscr{D}_\epsilon \text{ and } \boldsymbol{x}_{\text{tip}} \in \mathscr{D}_m, \\ \overline{\boldsymbol{C}}(\boldsymbol{x}), & \text{if } \boldsymbol{x} \in \mathscr{D} \setminus \mathscr{D}_\epsilon \end{cases} \tag{18}$$

where $\mathscr{D}_\epsilon \subset \mathscr{D}$ is a small bounded subdomain surrounding the crack tip, and $\mathscr{D}_p \subset \mathscr{D}$ and $\mathscr{D}_m \subset \mathscr{D}$ are particle and matrix subdomains, respectively. According to Eq. (18), discrete material properties of either the particle ($\boldsymbol{C}^{(p)}$) or the matrix ($\boldsymbol{C}^{(m)}$) are assigned to a small subdomain surrounding the crack tip and continuously varying effective material properties ($\overline{\boldsymbol{C}}(\boldsymbol{x})$) are defined on elsewhere, as shown in Fig. 2b. Therefore, discontinuities in material properties exist at the boundary of $\mathscr{D}_\epsilon$.

Since the material representation is locally homogeneous, i.e., $\boldsymbol{C}(\boldsymbol{x})$ is either $\boldsymbol{C}^{(p)}$ or $\boldsymbol{C}^{(m)}$, but constant for $\boldsymbol{x} \in \mathscr{D}_\epsilon$, the mixed-mode SIFs can be calculated from the interaction integral applicable to homogeneous materials. If the crack-tip contour is restricted to lie inside $\mathscr{D}_\epsilon$, the interaction integral for a locally homogeneous material [5], $M^{(1,2)}$, can be easily calculated. The interaction integral $M^{(1,2)}$ is different when

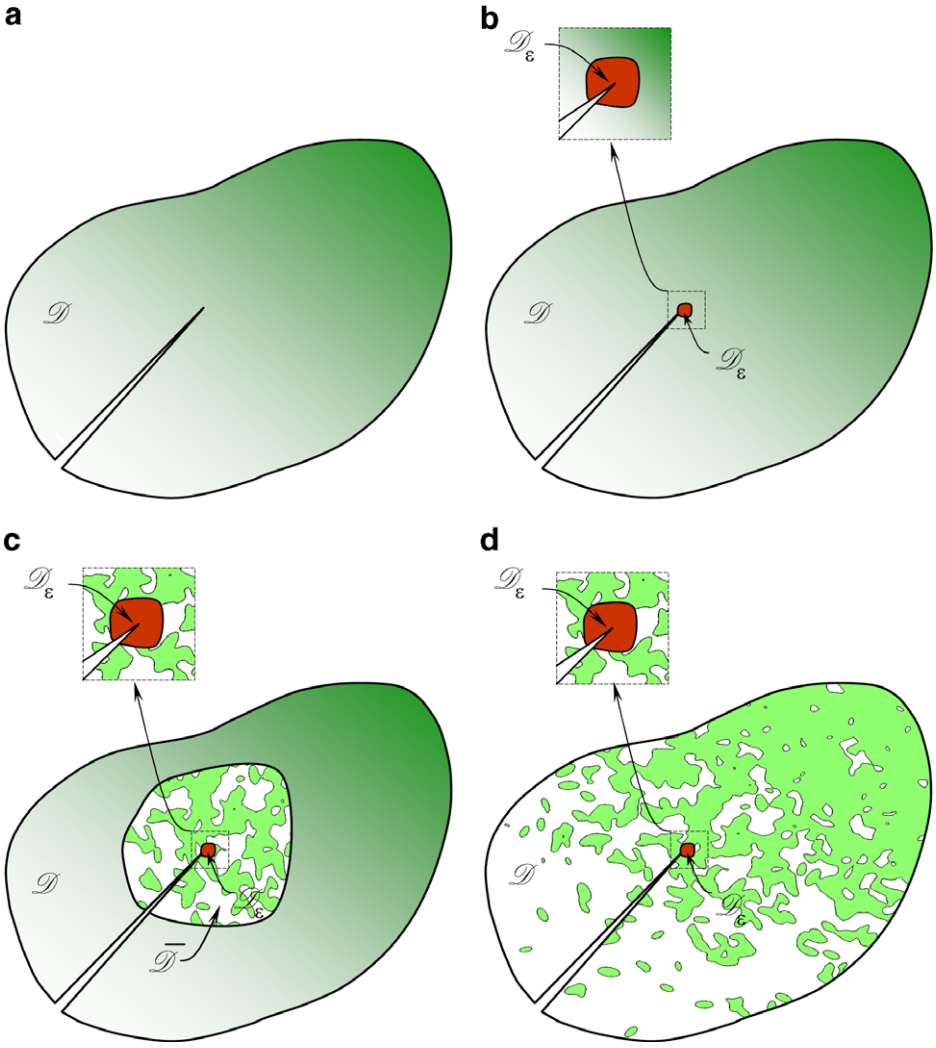

Fig. 2. Schematics of various models: (a) sequential multiscale; (b) invasive multiscale; (c) concurrent multiscale; (d) microscale. Note: $\mathscr{D}$ = domain of the entire solid, $\overline{\mathscr{D}}$ = subdomain with explicit particle information, $\mathscr{D}_\epsilon$ = small subdomain surrounding crack tip.

$\boldsymbol{C}(\boldsymbol{x}) = \boldsymbol{C}^{(p)}; \boldsymbol{x} \in \mathscr{D}_\epsilon$, e.g., $M_p^{(1,2)}$ and when $\boldsymbol{C}(\boldsymbol{x}) = \boldsymbol{C}^{(m)}; \boldsymbol{x} \in \mathscr{D}_\epsilon$, e.g., $M_m^{(1,2)}$. Then, the SIFs can be calculated from

$$K_i \cong \begin{cases} \frac{1}{2} M_p^{(1,i)} E_p^*, & \text{if } \boldsymbol{x}_{\text{tip}} \in \mathscr{D}_p \\ \frac{1}{2} M_m^{(1,i)} E_m^*, & \text{if } \boldsymbol{x}_{\text{tip}} \in \mathscr{D}_m \end{cases}; \quad i = \text{I, II.} \tag{19}$$

Compared with the sequential (Eq. (16)) and weighted sequential (Eq. (17)) models, the invasive model (Eq. (19)) utilizes more accurate crack-tip conditions and hence should provide improved estimates of SIFs over the two former models. However, it is unclear whether the improvements in the invasive model are adequate for calculating the failure probability of an FGM.

Two separate stochastic analyses, one with the crack tip in the particle phase and the other with the crack tip in the matrix phase, are required in the invasive model. In each stochastic analysis, $N = M + 4$ random variables are involved and, therefore, and correspondingly, $\boldsymbol{R} = \{Z_{p,1}, \ldots, Z_{p,M}, E_p, E_m, \nu_p, \nu_m\}^{\mathrm{T}} \in \mathbb{R}^N$. The probabilistic results from both stochastic analyses are weighted based on the particle volume fraction at the crack tip, leading to statistical properties of SIFs.

3.1.3. Concurrent multiscale model

The concurrent model includes both continuous and discrete material representations and requires a combined micromechanical and macromechanical stress analysis. Depicted in Fig. 2c, consider an arbitrary bounded subdomain $\overline{\mathscr{D}} \subseteq \mathscr{D}$, which contains a finite number of particles embedded in the matrix. The number of particles falling in $\overline{\mathscr{D}}$ is $\overline{\mathscr{N}} := \mathscr{N}(\overline{\mathscr{D}}')$, where $\overline{\mathscr{D}}' \subset \mathbb{R}^2$ is a bounded subset such that points of $\overline{\mathscr{N}}$ falling in $\mathbb{R}^2 \setminus \overline{\mathscr{D}}'$ do not contribute to particles in $\overline{\mathscr{D}}$. The integer-valued random variable $\overline{\mathscr{N}}$ also follows a Poisson distribution with the same intensity function $\lambda(\boldsymbol{x})$ derived from Eq. (8). The subdomain $\overline{\mathscr{D}}$, once defined, is statistically filled with particles in the matrix, and the remaining subdomain $\mathscr{D} \setminus \overline{\mathscr{D}}$ is assigned a continuously varying effective elasticity tensor $\overline{\boldsymbol{C}}(\boldsymbol{x})$, derived from a suitable micromechanical homogenization as in previous multiscale models. According to the concurrent model, Eq. (4) is discretized and solved using

$$\boldsymbol{C}(\boldsymbol{x}) \cong \begin{cases} \boldsymbol{C}^{(p)}, & \text{if } \boldsymbol{x} \in \overline{\mathscr{D}} \text{ and } \boldsymbol{x} \in \mathscr{D}_p \\ \boldsymbol{C}^{(m)}, & \text{if } \boldsymbol{x} \in \overline{\mathscr{D}} \text{ and } \boldsymbol{x} \in \mathscr{D}_m \\ \overline{\boldsymbol{C}}(\boldsymbol{x}), & \text{if } \boldsymbol{x} \in \mathscr{D} \setminus \overline{\mathscr{D}} \end{cases}. \tag{20}$$

Therefore, discontinuities in material properties exist at the interfaces between $\overline{\mathscr{D}}$ and $\mathscr{D} \setminus \overline{\mathscr{D}}$ and between $\mathscr{D}_p$ and $\mathscr{D}_m$.

Since the material representation in $\overline{\mathscr{D}}$ is discrete, the calculation of the resulting SIFs in the concurrent model is not straightforward. The interaction integral $\widetilde{M}$ or M, conveniently exploited in the former multiscale models, requires either continuously varying or constant material properties inside the domain of a crack-tip contour. However, if the idea of the small subdomain $\mathscr{D}_\epsilon \subset \overline{\mathscr{D}} \subseteq \mathscr{D}$, introduced in Section 3.1.2, is borrowed in slightly modifying the elasticity tensor, for instance

$$\boldsymbol{C}(\boldsymbol{x}) \cong \begin{cases} \boldsymbol{C}^{(p)}, & \text{if } (\boldsymbol{x} \in \mathscr{D}_\epsilon \text{ and } \boldsymbol{x}_{\text{tip}} \in \mathscr{D}_p) \text{ or if } (\boldsymbol{x} \in \overline{\mathscr{D}} \setminus \mathscr{D}_\epsilon \text{ and } \boldsymbol{x} \in \mathscr{D}_p) \\ \boldsymbol{C}^{(m)}, & \text{if } (\boldsymbol{x} \in \mathscr{D}_\epsilon \text{ and } \boldsymbol{x}_{\text{tip}} \in \mathscr{D}_m) \text{ or if } (\boldsymbol{x} \in \overline{\mathscr{D}} \setminus \mathscr{D}_\epsilon \text{ and } \boldsymbol{x} \in \mathscr{D}_m), \\ \overline{\boldsymbol{C}}(\boldsymbol{x}), & \text{if } \boldsymbol{x} \in \mathscr{D} \setminus \overline{\mathscr{D}} \end{cases} \tag{21}$$

the material representation in the concurrent model remains locally homogeneous, rendering the interaction integral method applicable. Applying Eq. (21) in solving the discretized weak form yields the M-integrals, $M_p^{(1,2)}$ and $M_m^{(1,2)}$, when $\boldsymbol{C}(\boldsymbol{x}) = \boldsymbol{C}^{(p)}; \boldsymbol{x} \in \mathscr{D}_\epsilon$ and $\boldsymbol{C}(\boldsymbol{x}) = \boldsymbol{C}^{(m)}; \boldsymbol{x} \in \mathscr{D}_\epsilon$, respectively. The SIFs are subsequently calculated using Eq. (19). Although the same fracture-mechanics equations are used, the SIFs obtained from the concurrent model should be different than those from the invasive model. This is because the M-integrals resulting from Eq. (21) (concurrent model) are different than those calculated from Eq. (18) (invasive model). The discrete particles in $\overline{\mathscr{D}}$, if they produce any effect, should influence the M-integrals obtained in the concurrent model. No such effect is accounted for in the invasive model. The magnitude of the effect, however, depends on the relative size of $\overline{\mathscr{D}}$. If the size of $\overline{\mathscr{D}}$ is shrunk to approach the size of $\mathscr{D}_\epsilon$, the concurrent model degenerates to the invasive model. If the size of $\overline{\mathscr{D}}$ is expanded to approach the size of $\mathscr{D}$, the model no longer remains a multiscale model, but becomes a uniscale model, which is explained in the next subsection.

The stochastic analysis employing the concurrent multiscale model has the random input vector $\boldsymbol{R} = \{Z_{p,1}, \ldots, Z_{p,M}, \overline{\mathscr{N}}, (U_{1,1}, U_{1,2}), \ldots, (U_{\overline{\mathscr{N}},1}, U_{\overline{\mathscr{N}},2}), E_p, E_m, \nu_p, \nu_m\}^{\mathrm{T}} \in \mathbb{R}^N$, where $N = M + 2\overline{\mathscr{N}} + 5$. It is worth noting that the number of Poisson points $\overline{\mathscr{N}}$ and, hence, the dimension N are integer-valued random variables.

3.2. Microscale analysis

The microscale model is a straightforward uniscale model, where $\mathscr{N}$ discrete particles are dispersed in the matrix, as shown in Fig. 2d. The number of particles falling in $\mathscr{D}'$ is $\mathscr{N}(\mathscr{D}')$, where $\mathscr{D}' \subset \mathbb{R}^2$ is a bounded subset such that the points of $\mathscr{N}$ falling in $\mathbb{R}^2 \setminus \mathscr{D}'$ do not contribute to the particles in $\mathscr{D}$. The integer-valued random variable $\mathscr{N}$ follows a Poisson distribution with the intensity function $\lambda(\boldsymbol{x})$ derived from Eq. (8). The domain $\mathscr{D}$ is statistically filled with particles in the matrix according to the steps outlined in Section 2.2.2. For the particle–matrix composite system, a microscale stress analysis is performed, where the elasticity tensor

$$\boldsymbol{C}(\boldsymbol{x}) \cong \begin{cases} \boldsymbol{C}^{(p)}, & \text{if } \boldsymbol{x} \in \mathscr{D}_p \\ \boldsymbol{C}^{(m)}, & \text{if } \boldsymbol{x} \in \mathscr{D}_m \end{cases} \tag{22}$$

is piecewise constant at $\boldsymbol{x} \in \mathscr{D}_p$ and $\boldsymbol{x} \in \mathscr{D}_m$, but discontinuous at the interfaces between $\mathscr{D}_p$ and $\mathscr{D}_m$. In contrast with the multiscale models, no effective properties are included or required.

The fracture-mechanics calculation of SIFs employing Eq. (22) and the interaction integral method poses the same problem encountered in the concurrent multiscale model. However, by introducing a small subdomain $\mathscr{D}_\epsilon \subset \mathscr{D}$, as done in the concurrent model, the modified elasticity tensor

$$\boldsymbol{C}(\boldsymbol{x}) \cong \begin{cases} \boldsymbol{C}^{(p)}, & \text{if } (\boldsymbol{x} \in \mathscr{D}_\epsilon \text{ and } \boldsymbol{x}_{\text{tip}} \in \mathscr{D}_p) \text{ or if } (\boldsymbol{x} \in \mathscr{D} \setminus \mathscr{D}_\epsilon \text{ and } \boldsymbol{x} \in \mathscr{D}_p) \\ \boldsymbol{C}^{(m)}, & \text{if } (\boldsymbol{x} \in \mathscr{D}_\epsilon \text{ and } \boldsymbol{x}_{\text{tip}} \in \mathscr{D}_m) \text{ or if } (\boldsymbol{x} \in \mathscr{D} \setminus \mathscr{D}_\epsilon \text{ and } \boldsymbol{x} \in \mathscr{D}_m) \end{cases} \tag{23}$$

also leads to a local homogenization; therefore, the M-integrals can be readily calculated. Subsequently, the SIFs are calculated by invoking Eq. (19). The effect of discrete particles in the entire domain $\mathscr{D}$ is propagated to the M-integrals obtained in the microscale model. Such effect is also accounted for in the concurrent multiscale model, but only from particles embedded in the subdomain $\overline{\mathscr{D}}$.

The stochastic analysis employing the microscale model has the random input vector $\boldsymbol{R} = \{Z_{p,1}, \ldots, Z_{p,M}, \mathscr{N}, (U_{1,1}, U_{1,2}), \ldots, (U_{\mathscr{N},1}, U_{\mathscr{N},2}), E_p, E_m, \nu_p, \nu_m\}^{\mathrm{T}} \in \mathbb{R}^N$, where $N = M + 2\mathscr{N} + 5$. Also, the number of Poisson points $\mathscr{N}$ and, hence, the dimension N are integer-valued random variables.

In summary, three multiscale models and a microscale model have been presented to solve the stochastic fracture-mechanics problem described in Section 2. The multiscale models employ effective material properties whenever possible and include further assumptions or approximations to help solve the problem economically. In contrast, the microscale model constitutes a brute-force approach that employs a discrete particle–matrix system to solve the problem as accurately as possible, considered in the present work. Therefore, the microscale model is the most expensive model studied, but it is required to evaluate the accuracy and efficiency of the multiscale models.

4. Stochastic analysis

Recall that $y(\boldsymbol{r}) = y(r_1, \ldots, r_N)$ represents either a crack-driving force or a performance function that depends on crack-driving forces. The number of input random variables N, the dimension of the stochastic problem, and the input–output mapping $y : \mathbb{R}^N \to \mathbb{R}$ depends on the multiscale or microscale method selected. Nonetheless, the objective is to evaluate the probabilistic characteristics of a generic output response $y(\boldsymbol{R}) \in \mathbb{R}^N$, when the probability distribution of the random input $\boldsymbol{R} \in \mathbb{R}^N$ is prescribed.

4.1. Dimensional decomposition method

Consider a continuous, differentiable, real-valued, multivariate function $y(\boldsymbol{r})$ that depends on $\boldsymbol{r} = \{r_1, \ldots, r_N\}^{\mathrm{T}} \in \mathbb{R}^N$. A dimensional decomposition of $y(\boldsymbol{r})$, described by [18,19]

$$\begin{aligned} y(\boldsymbol{r}) = y_0 + \sum_{i=1}^{N} y_i(r_i) + \sum_{i_1, i_2 = 1; i_1 < i_2}^{N} y_{i_1 i_2}(r_{i_1}, r_{i_2}) + \cdots + \sum_{i_1, \ldots, i_S = 1; i_1 < \cdots < i_S}^{N} y_{i_1 \cdots i_S}(r_{i_1}, \ldots, r_{i_s}) + \cdots \\ + y_{12\cdots N}(r_1, \ldots, r_N), \end{aligned} \tag{24}$$

can be viewed as a finite hierarchical expansion of an output function in terms of its input variables with increasing dimensions, where y_0 is a constant, $y_i(r_i)$ is a univariate component function representing individual contribution to $y(\boldsymbol{r})$ by input variable r_i acting alone, $y_{i_1 i_2}(r_{i_1}, r_{i_2})$ is a bivariate component function describing the cooperative influence of two input variables r_{i_1} and r_{i_2}, $y_{i_1 \cdots i_S}(r_{i_1}, \ldots, r_{i_S})$ is an S-variate component function quantifying cooperative effects of S input variables $r_{i_1}, \ldots, r_{i_S}$, and so on. If

$$\hat{y}_S(\boldsymbol{r}) = y_0 + \sum_{i=1}^{N} y_i(r_i) + \sum_{i_1, i_2 = 1; i_1 < i_2}^{N} y_{i_1 i_2}(r_{i_1}, r_{i_2}) + \cdots + \sum_{i_1, \ldots, i_S = 1; i_1 < \cdots < i_S}^{N} y_{i_1 \cdots i_S}(r_{i_1}, \ldots, r_{i_s}) \tag{25}$$

represents a general S-variate approximation of $y(\boldsymbol{r})$, the univariate ($S=1$) and bivariate ($S=2$) approximations $\hat{y}_1(\boldsymbol{r})$ and $\hat{y}_2(\boldsymbol{r})$, respectively, provide two- and three-term approximants of the finite decomposition in Eq. (24). When $S=N$, $\hat{y}_S(\boldsymbol{r})$ converges to the exact function $y(\boldsymbol{r})$, i.e., Eq. (25) generates a hierarchical and convergent sequence of approximations of $y(\boldsymbol{r})$.

4.1.1. Lower-variate approximations

Consider the univariate and bivariate approximations of $y(\boldsymbol{r})$, defined by

$$\hat{y}_1(\boldsymbol{r}) := \hat{y}_1(r_1,\ldots,r_N) := \sum_{i=1}^{N} y(c_1,\ldots,c_{i-1},r_i,c_{i+1},\ldots,c_N) - (N-1)y(\boldsymbol{c}) \tag{26}$$

and

$$\begin{aligned}\hat{y}_2(\boldsymbol{r}) := \hat{y}_2(r_1,\ldots,r_N) := & \sum_{i_1,i_2=1;i_1<i_2}^{N} y(c_1,\ldots,c_{i_1-1},r_{i_1},c_{i_1+1},\ldots,c_{i_2-1},r_{i_2},c_{i_2+1},\ldots,c_N) \\ & + \sum_{i=1}^{N} -(N-2)y(c_1,\ldots,c_{i-1},r_i,c_{i+1},\ldots,c_N) + \frac{(N-1)(N-2)}{2}y(\boldsymbol{c}),\end{aligned} \tag{27}$$

respectively, where $\boldsymbol{c}=\{c_1,\ldots,c_N\}^{\mathrm{T}}$ is the mean point of $\boldsymbol{R}$, $y(\boldsymbol{c}) := y(c_1,\ldots,c_N)$ is a constant, and $y_i(r_i) := y(c_1,\ldots,c_{i-1},r_i,c_{i+1},\ldots,c_N)$ and $y_{i_1i_2}(r_{i_1},r_{i_2}) := y(c_1,\ldots,c_{i_1-1},r_{i_1},c_{i_1+1},\ldots,c_{i_2-1},r_{i_2},c_{i_2}+1,\ldots,c_N)$ are univariate and bivariate component functions, respectively. All higher-order univariate or bivariate terms of $y(\boldsymbol{r})$ are included in Eqs. (26) or (27), which should, therefore, generally provide a higher-order approximation of a multivariate function than equations derived from first- or second-order Taylor expansions.

4.1.2. Lagrange interpolations

Since $y_i(r_i)$ and $y_{i_1i_2}(r_{i_1},r_{i_2})$ are lower-variate functions, they can be further approximated by n-point Lagrange interpolations, leading to

$$y_i(r_i) = \sum_{j=1}^{n} \zeta_j(r_i) y(c_1,\ldots,c_{i-1},r_i^{(j)},c_{i+1},\ldots,c_N) \tag{28}$$

and

$$y_{i_1i_2}(r_{i_1},r_{i_2}) = \sum_{j_2=1}^{n}\sum_{j_1=1}^{n} \zeta_{j_1}(r_{i_1})\zeta_{j_2}(r_{i_2}) y\left(c_1,\ldots,c_{i_1-1},r_{i_1}^{(j_1)},c_{i_1+1},\ldots,c_{i_2-1},r_{i_2}^{(j_2)},c_{i_2+1},\ldots,c_N\right), \tag{29}$$

where $\zeta_j(r_i) := \prod_{k=1,k\neq j}^{n}(r_i - r_i^{(k)})/\prod_{k=1,k\neq j}^{n}(r_i^{(j)} - r_i^{(k)})$ is the Lagrange shape function and $r_i^{(j)}$ is the jth sample point of r_i. The procedure is repeated for all univariate and bivariate component functions, i.e., for all $y_i(r_i)$, $i=1,\ldots,N$ and for all $y_{i_1i_2}(r_{i_1},r_{i_2}), i_1,i_2=1,\ldots,N$, leading to the univariate approximation

$$\hat{y}_1(\boldsymbol{R}) = \sum_{i=1}^{N}\sum_{j=1}^{n} \zeta_j(R_i) y(c_1,\ldots,c_{i-1},r_i^{(j)},c_{i+1},\ldots,c_N) - (N-1)y(\boldsymbol{c}), \tag{30}$$

and to the bivariate approximation

$$\begin{aligned}\hat{y}_2(\boldsymbol{R}) = & \sum_{i_1,i_2=1;i_1<i_2}^{N}\sum_{j_2=1}^{n}\sum_{j_1=1}^{n} \zeta_{j_1}(R_{i_1})\zeta_{j_2}(R_{i_2}) \times y(c_1,\ldots,c_{i_1-1},r_{i_1}^{(j_1)},c_{i_1+1},\ldots,c_{i_2-1},r_{i_2}^{(j_2)},c_{i_2+1},\ldots,c_N) \\ & - (N-2)\sum_{i=1}^{N}\sum_{j=1}^{n} \zeta_j(R_i) y(c_1,\ldots,c_{i-1},r_i^{(j)},c_{i+1},\ldots,c_N) + \frac{(N-1)(N-2)}{2}y(\boldsymbol{c}).\end{aligned} \tag{31}$$

4.1.3. Monte carlo simulation

Once the Lagrange shape functions and coefficients $y(\boldsymbol{c})$, $y(c_1,\ldots,c_{i-1},r_i^{(j)},c_{i+1},\ldots,c_N)$, and $y(c_1,\ldots,c_{i_1-1},r_{i_1}^{(j_1)},c_{i_1+1},\ldots,c_{i_2-1},r_{i_2}^{(j_2)},c_{i_2+1},\ldots,c_N)$ are deterministically generated, Eqs. (30) and (31) provide explicit approximations of a crack-driving force or a performance function ($y(\boldsymbol{R})$) in terms of the random input $\boldsymbol{R}$. Therefore, many probabilistic characteristics of $y(\boldsymbol{R})$, including its statistical moments and probability density function, can be easily evaluated by performing Monte Carlo simulation on Eqs. (30) and (31). Since Eqs. (30) and (31) do not require performing additional finite-element analysis, the embedded Monte Carlo simulation can be efficiently conducted for any sample size. The stochastic methods involving the univariate (Eq. (30)) or bivariate (Eq. (31)) approximations and associated Monte Carlo simulation are defined as the *univariate* or *bivariate decomposition methods* in this paper.

4.2. Direct monte carlo simulation

Consider a generic N-dimensional random vector $\boldsymbol{R}=\{R_1,\ldots,R_N\}^{\mathrm{T}}$, which characterizes uncertainty in all input parameters under consideration with its known joint PDF $f_{\boldsymbol{R}}(\boldsymbol{r})$. Suppose that $\boldsymbol{r}^{(1)},\ldots,\boldsymbol{r}^{(L)}$ are L realizations of the input vector $\boldsymbol{R}$, which can be generated independently. Let $y(\boldsymbol{r}^{(1)}),\ldots,y(\boldsymbol{r}^{(L)})$ be the output samples of a relevant crack-driving force or performance function $y(\boldsymbol{R})$ that correspond to the input $\boldsymbol{r}^{(1)}$, …, $\boldsymbol{r}^{(L)}$, which can be obtained from repeated deterministic fracture-mechanics evaluations of y. The direct Monte Carlo estimate $P_{\mathrm{F,MCS}}$ of the failure probability is [20]

$$P_{\mathrm{F,MCS}}(K_{\mathrm{Ic}})=\lim_{L\to\infty}\frac{1}{L}\sum_{i=1}^{L}\mathbb{I}_y(\boldsymbol{r}^{(i)}), \tag{32}$$

where $\mathbb{I}_y(\boldsymbol{r}^{(i)})$ denotes the ith realization of the indicator function defined in Eq. (11).

The direct Monte Carlo simulation in Eq. (32) should not be confused with the Monte Carlo simulation in the decomposition method. The direct Monte Carlo simulation, which requires finite-element calculations of $y(\boldsymbol{r}^{(i)})$ for any input sample $\boldsymbol{r}^{(i)}$, can be expensive or even prohibitive, particularly when the sample size L needs to be very large for estimating small failure probabilities. In contrast, the Monte Carlo simulation embedded in the decomposition method requires evaluations of simple analytical functions that stem from either the univariate ($\hat{y}_1(\boldsymbol{r}^{(i)})$) or bivariate ($\hat{y}_2(\boldsymbol{r}^{(i)})$) approximations of $y(\boldsymbol{r}^{(i)})$. Therefore, an arbitrarily large sample size can be accommodated in the decomposition method.

Both the decomposition and direct Monte Carlo simulation methods are required for solving the stochastic fracture problem examined in this work. The sequential and invasive multiscale models have a total number of random variables $N=M+4$, which is deterministic, and do not require discrete particle distributions in the matrix. Therefore, the dimensional decomposition method can be applied to the associated stochastic analysis. In contrast, the concurrent multiscale model and the microscale model have a random number of random variables (e.g., $N=M+2\overline{\mathscr{N}}+5$ or $N=M+2\mathscr{N}+5$). More importantly, the models require stress analyses involving discrete particle–matrix systems where the location of any particle is uniformly distributed over $\overline{\mathscr{D}}'$ or $\mathscr{D}'$. Therefore, calculating the coefficient $y(\boldsymbol{c})$, a response at mean input, involves fracture analysis, where all particle locations coincide at the center of $\overline{\mathscr{D}}'$ or $\mathscr{D}'$. Similar problems occur when calculating the remaining coefficients of the decomposition method. Consequently, for the two latter models, the decomposition method in the current form can not propagate the uncertainty due to discrete particle locations to crack-driving forces. Hence, the direct Monte Carlo simulation was employed for stochastic analyses associated with the concurrent multiscale and microscale models.

5. A numerical example

5.1. Problem definition

Consider a 16 cm × 16 cm, two-dimensional, square, FGM specimen, which contains randomly dispersed, fully penetrable, circular, silicon carbide (SiC) particles in an aluminum (Al) matrix, as shown in Fig. 3. All particles have the same size with a common radius of 0.48 cm. The specimen contains a horizontally placed,

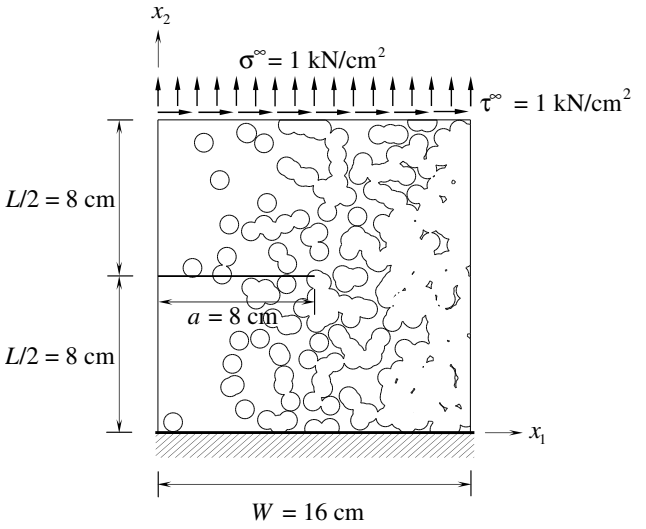

Fig. 3. An FGM specimen with an edge crack under a mixed-mode deformation.

8-cm – long edge crack with the initial crack tip location $\boldsymbol{x}_{\text{tip}} = \{x_{\text{tip},1}, x_{\text{tip},2}\}^{\text{T}} = \{8, 8\}^{\text{T}}$ cm and is subjected to a far-field tensile stress $\sigma^\infty = 1$ kN/cm^2 and a far-field shear stress $\tau^\infty = 1$ kN/cm^2. The subdomain $\mathscr{D}'$ is a 16.96 cm $\times$ 16.96 cm square with the center coinciding with that of $\mathscr{D}$. The subdomain $\mathscr{D}_\epsilon$ is a circle with radius of 0.24 cm and the center at the crack tip. The subdomain $\overline{\mathscr{D}}$ is a 16κ cm $\times$ 16κ cm^2 with the center coinciding with the crack tip, where κ represents the ratio of the areas of $\overline{\mathscr{D}}$ and $\mathscr{D}$. The subdomain $\overline{\mathscr{D}}'$ is a $16\kappa + 0.96$ cm $\times$ 16κ+0.96 cm^2 with the center coinciding with that of $\overline{\mathscr{D}}$. In the present work two values of κ were used: i.e., $\kappa = 0.25$ or 0.5. A plane strain condition was assumed.

The particle volume fraction $\phi_p(x_1)$, which varies along the horizontal coordinate, is a one-dimensional, inhomogeneous, Beta random field. It has a marginal PDF $[1/B(q,t)]\phi_p^{q-1}(1-\phi_p)^{t-1}$, where $B(q, t) := \Gamma(q)\Gamma(t)/\Gamma(q+t)$ is the Beta function and $\Gamma(\tau) := \int_0^\infty \exp(-\eta)\eta^{\tau-1}\,\mathrm{d}\eta$ is the Gamma function. The random field $\phi_p(x_1)$ has mean $\mu_p(x_1) = \bar{x}_1$ and standard deviation $\sigma_p(x_1) = 0.1\bar{x}_1(1-\bar{x}_1)$, where $\bar{x}_1 = x_1/W$. The standardized volume fraction $\tilde{\phi}_p(x_1)$, a Beta random field with *zero* mean and *unit* variance, has covariance function $\Gamma_{\tilde{\phi}_p}(s) = \exp(-5|s|)$. The Karhunen–Loève approximation was employed to parameterize the Gaussian image field $\alpha(x_1)$ of $\tilde{\phi}_p(x_1)$ into eight ($M = 8$) standard Gaussian random variables $Z_{p,1}, \ldots, Z_{p,8}$. The Karhunen–Loève expansion was truncated after eight terms, because the eighth eigenvalue is only 4.5% of the maximum eigenvalue.

For a given sample $\varphi_p(x_1)$ of the random volume fraction $\phi_p(x_1)$, the corresponding numbers of particles $\mathscr{N}$ and $\overline{\mathscr{N}}$ in $\mathscr{D}\prime$ and $\overline{\mathscr{D}}\prime$, respectively, are both Poisson variables and have the same intensity function $\lambda(x_1)$ that was obtained from Eq. (8). The sets of uniformly distributed random variables $(U_{1,1}, U_{1,2}), \ldots, (U_{\mathscr{N},1}, U_{\mathscr{N},2})$ and $(U_{1,1}, U_{1,2}), \ldots, (U_{\overline{\mathscr{N}},1}, U_{\overline{\mathscr{N}},2})$ describe random particle locations in $\mathscr{D}$ and $\overline{\mathscr{D}}$, respectively. Finally, the material phases SiC and Al are both linear-elastic and isotropic. However, the elastic moduli E_{SiC} and E_{Al} and the Poisson's ratios ν_{SiC} and ν_{Al}, of SiC and Al, respectively, are random variables; their means, standard deviations, and probability distributions are listed in Table 1. For stochastic analysis by the dimensional

Table 1
Statistical properties of constituents in SiC–Al FGM

Elastic property[a]	Mean	Coefficient of variation, %	Probability distribution
E_{SiC}, GPa	419.2	15	Lognormal
E_{Al}, GPa	69.7	10	Lognormal
ν_{SiC}	0.19	15	Lognormal
ν_{Al}	0.34	10	Lognormal

[a] $E_p = E_{\text{SiC}}$; $E_m = E_{\text{Al}}$; $\nu_p = \nu_{\text{SiC}}$; $\nu_m = \nu_{\text{Al}}$.

decomposition method, $N = 12$ and $n = 5$. The sample size for both the decomposition and direct Monte Carlo simulation was 10,000.

5.2. Results and discussion

Figs. 4a–d present four finite-element discretizations of a sample of the FGM specimen employed in conjunction with the sequential or weighted sequential, invasive, concurrent, and microscale models, respectively. For the sequential or weighted sequential model, the finite-element mesh for $\mathscr{D}$ involves 1328 eight-noded, non-singular, quadrilateral elements and 48 six-noded, quarter-point (singular), triangular elements at the crack tip. The mesh for the invasive model comprises 1560 eight-noded, non-singular, quadrilateral elements and 8 six-noded, non-singular, triangular elements in $\mathscr{D} \setminus \mathscr{D}_\epsilon$, and 72 eight-noded, non-singular, quadrilateral elements and 8 eight-noded, quarter-point (singular), collapsed quadrilateral elements in $\mathscr{D}_\epsilon$. The mesh for the concurrent model has 1762 eight-noded, non-singular, quadrilateral elements in $\mathscr{D} \setminus \overline{\mathscr{D}}$ and 3584 six-noded, non-singular, triangular elements in $\overline{\mathscr{D}} \setminus \mathscr{D}_\epsilon$, and 72 eight-noded, non-singular, quadrilateral elements and 8 eight-noded, quarter-point (singular), collapsed quadrilateral elements in $\mathscr{D}_\epsilon$. Finally, the mesh for the microscale model includes 17,456 six-noded, non-singular, triangular elements in $\mathscr{D} \setminus \mathscr{D}_\epsilon$ and 72 eight-noded, non-singular, quadrilateral elements and 8 eight-noded, quarter-point (singular), collapsed quadrilateral elements in $\mathscr{D}_\epsilon$. All finite-element meshes are conforming and were developed using an in-house computer code for the sequential or weighted sequential model, or the commercial code ABAQUS [21] for the remaining models. Full 3×3 and 3-point Gauss quadrature rules were employed for the quadrilateral and triangular elements, respectively, for the numerical integration.

Figs. 5a–d plot von Mises stress contours for the same FGM sample, generated from the sequential or weighted sequential, invasive, concurrent, and microscale models, respectively. The effective properties required by all multiscale models were calculated using the Mori–Tanaka approximation. The overall stress responses from all multiscale and microscale models, indicated by the contour patterns, are similar. However, there are also differences in the local stress fields that may have significant implications in determining crack-driving forces and eventually in reliability predictions by various models. The results pertaining to fracture response and reliability are presented next.

5.2.1. Verification of the decomposition methods

Of the two stochastic methods employed, the dimensional decomposition method is significantly more computationally inexpensive than the direct Monte Carlo simulation, but the former method provides approximate results. Therefore, any probabilistic result from the decomposition method requires a verification, which Fig. 6a delivers in comparing the marginal PDFs of K_{I} and K_{II} by the decomposition and direct Monte Carlo methods employing the sequential multiscale model. The probability densities obtained by the univariate and bivariate decomposition methods are in close agreement with the histograms generated by the direct Monte Carlo simulation employing the sequential multiscale model. The bivariate method is slightly more accurate than the univariate method. Computationally, the univariate and bivariate methods, using $N = 12$ and $n = 5$, require only 49 and 1105 finite-element analyses, respectively, whereas 10,000 finite-element analyses were conducted in the direct Monte Carlo method. Therefore, the decomposition methods are not only accurate, but also computationally inexpensive. The probability densities of K_{I} and K_{II} obtained using the weighted sequential multiscale model, exhibited in Fig. 6b, support the same conclusion in terms of both the accuracy and the efficiency of the decomposition methods. A similar comparison entailing the invasive model was also made, but it is not reported here for brevity. However, the decomposition method in its current form cannot solve the stochastic fracture problem using either the concurrent model or the microscale model. Hence, the direct Monte Carlo simulation is needed and was employed in the latter two models. All forthcoming probabilistic results are based on the bivariate decomposition method for the sequential, weighted sequential, and invasive models, and the direct Monte Carlo simulation for the concurrent and microscale models.

5.2.2. Crack-driving forces

Table 2 lists the second-moment statistics of K_{I} and K_{II} by various multiscale and microscale models examined in this work. Among various models, the statistics from the microscale model, which requires the fewest

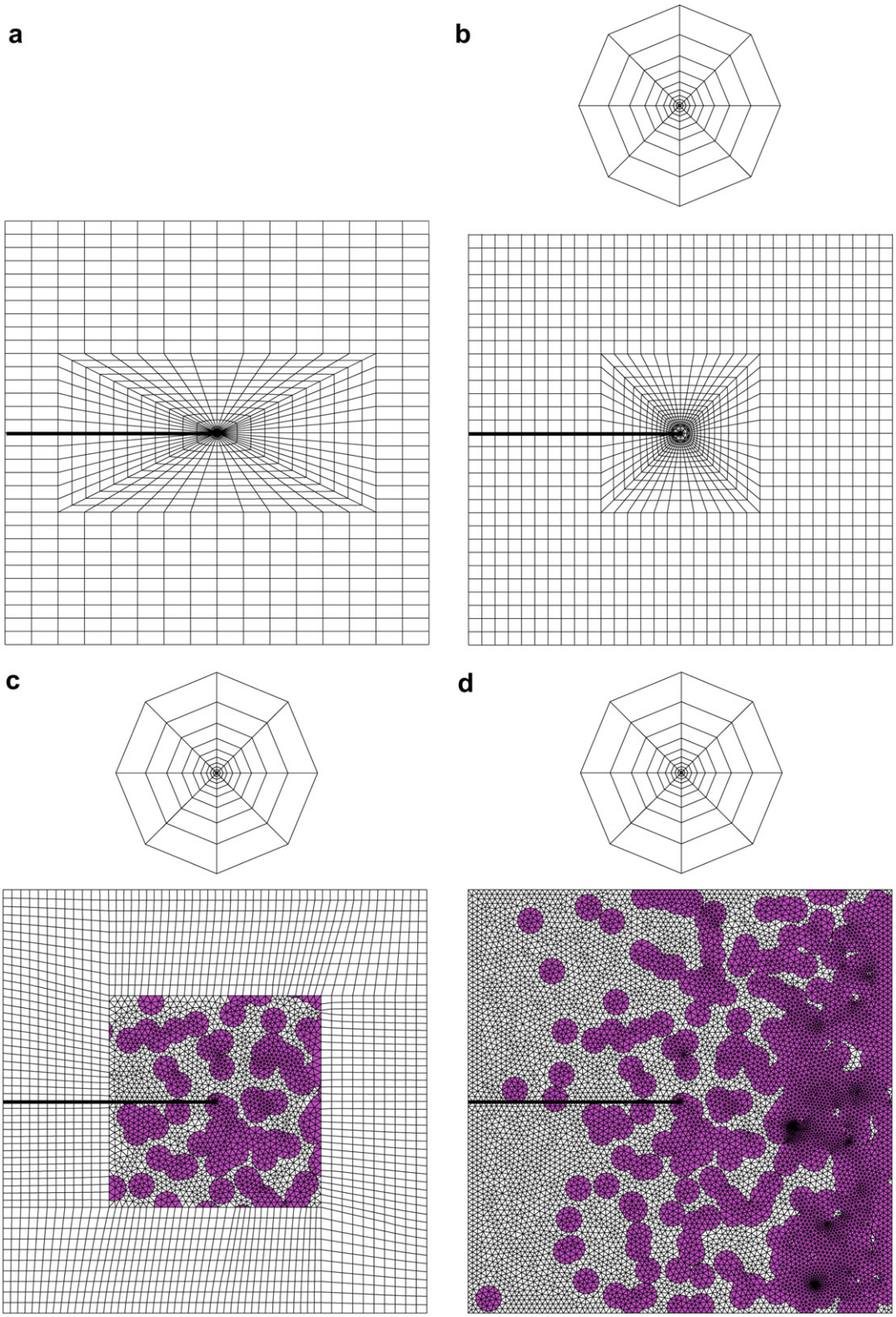

Fig. 4. Finite-element discretizations for a sample specimen: (a) sequential or weighted sequential multiscale: (b) invasive multiscale; (c) concurrent multiscale; (d) microscale.

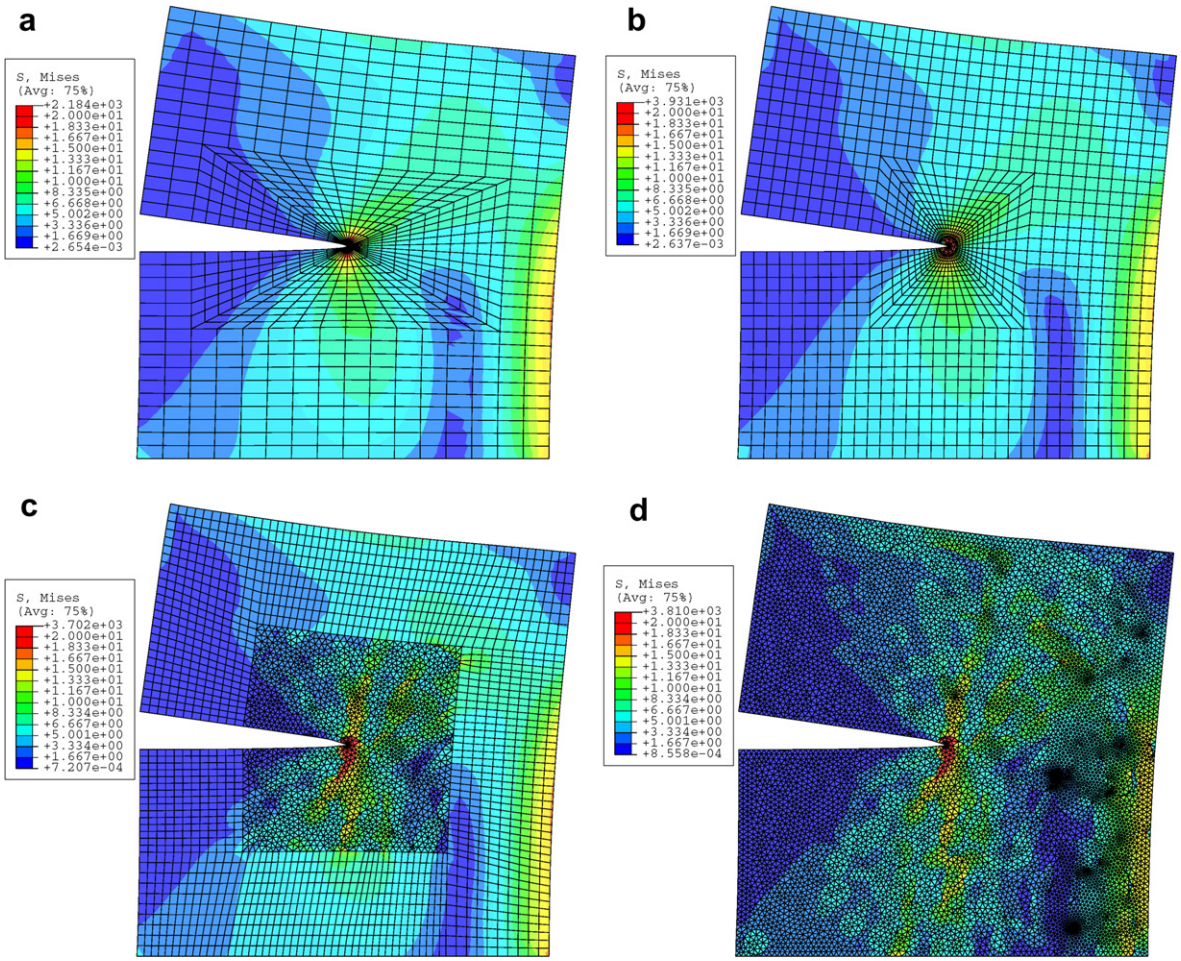

Fig. 5. von Mises stress contours for a sample specimen: (a) sequential or weighted sequential multiscale; (b) invasive multiscale; (c) concurrent multiscale; (d) microscale.

approximations, were treated as the reference solutions. From Table 2, the sequential, weighted sequential, and invasive models show reasonably good agreement when comparing the mean values of K_{I} and K_{II} with those of the reference model, except for the mean value of K_{II} employing the weighted sequential model.

The concurrent model with $\kappa = 0.25$ or $\kappa = 0.5$ provides better estimates of the means of SIFs than any other multiscale models. The superior accuracy of the concurrent model extends to evaluating the standard deviations of SIFs, which are significantly underpredicted by all other multiscale models except the invasive model, which predicts the standard deviation of K_{I} accurately. The accuracy of the concurrent models slightly improves when κ is larger, e.g., $\kappa = 0.5$, as expected.

While the second-moment statistics are useful, a more meaningful stochastic response is the PDF of a SIF. Figs. 7a and b present predicted probability densities of K_{I}, obtained from two groups of models: the sequential, weighted sequential, and invasive models; and the concurrent models with $\kappa = 0.25$ or $\kappa = 0.5$, respectively. In each group, the probability density of K_{I} from the microscale model was employed to evaluate the PDFs from the multiscale models. The PDF of K_{I} from the microscale model reveals a bimodal shape, where the left and right parts of the density are due to major contributions from the matrix and particle phases, respectively. From Fig. 7a, the sequential and weighted sequential models produce unimodal PDFs, and hence both models fail to capture the essential bimodal character. The invasive model, due to an explicit introduction of the particle or matrix phases in $\mathscr{D}_\epsilon$ locally, picks up the bimodal shape, but the results are still not close to the PDF generated by the microscale model. A lack of particles and their location variability,

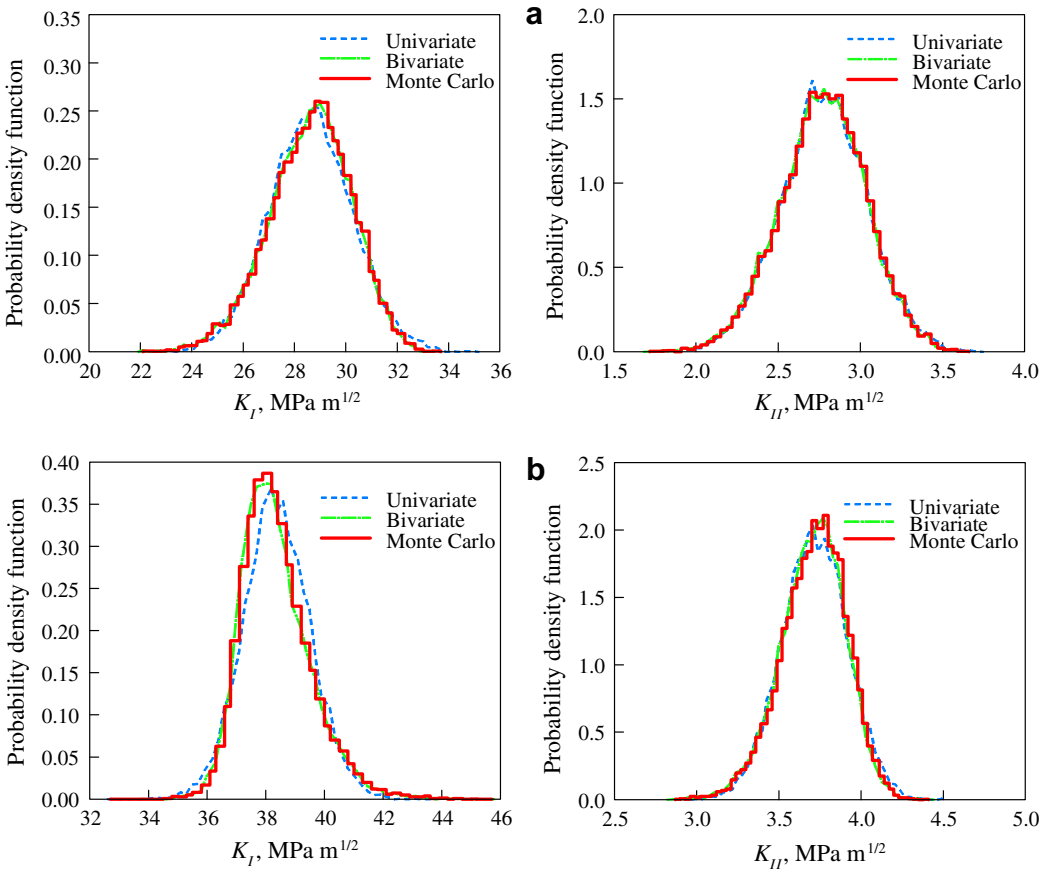

Fig. 6. Verification of the decomposition method for calculating PDFs of K_I and K_{II}: (a) sequential; (b) weighted sequential.

Table 2
Second-moment statistics of stress-intensity factors by various models

Model	K_I, MPa$\sqrt{m}$		K_{II}, MPa$\sqrt{m}$	
	Mean	Standard deviation	Mean	Standard deviation
Sequential[a]	28.604	1.609	2.770	0.263
Weighted sequential[a]	38.338	1.191	3.705	0.199
Invasive[a]	29.887	13.280	2.487	0.939
Concurrent ($\kappa = 0.25$)[b]	30.095	13.083	2.200	2.250
Concurrent ($\kappa = 0.5$)[b]	30.961	13.469	2.232	2.306
Microscale[b]	32.213	13.998	2.191	2.391

[a] Using bivariate decomposition method; $N = 12$; $n = 5$; $L = 10{,}000$.
[b] Using direct Monte Carlo simulation; $L = 10{,}000$.

except at the crack tip, is the major reason for the disparity of results between the invasive and the microscale models. In contrast, the concurrent models, using either $\kappa = 0.25$ or $\kappa = 0.5$, in Fig. 7b provide markedly improved estimates of the PDF compared with any other multiscale model. This is because the explicit presence of particle or matrix phases at the crack-tip and particle distributions in the crack-tip region have been adequately accounted for in the concurrent models.

The probability densities of K_{II}, obtained by various models and organized similarly, are displayed in Figs. 8a and b. The PDF of K_{II} from the microscale model is unimodal and, therefore, different than that of K_I.

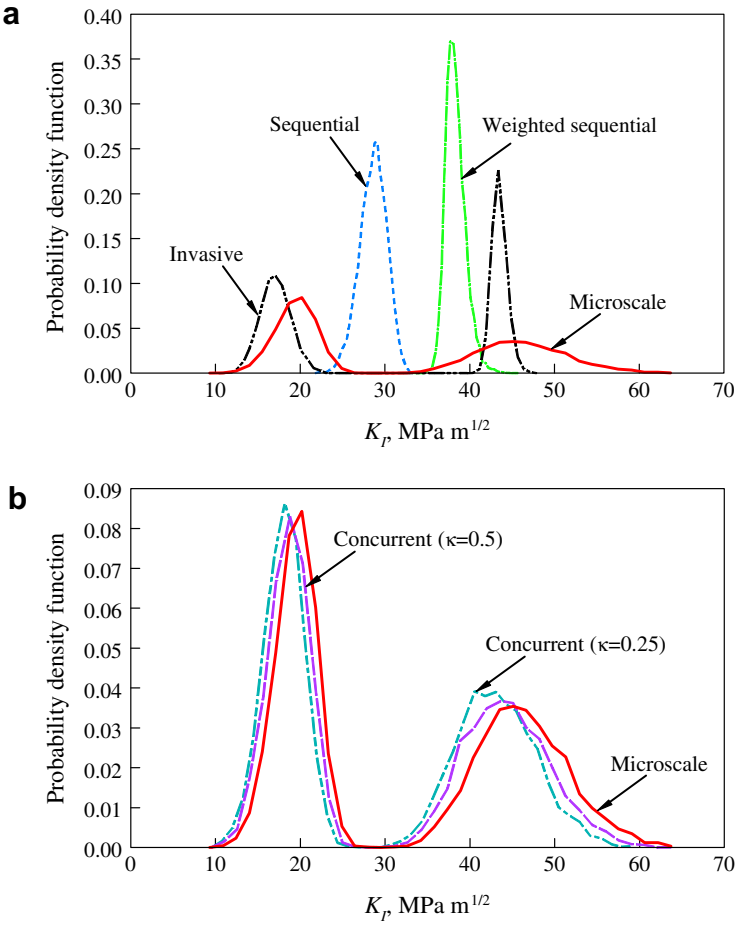

Fig. 7. PDFs of K_I by various models: (a) simpler multiscale models; (b) concurrent model.

Since the problem studied here is dominated by mode-I and the mean value of K_{II} is relatively closer to zero, the particle distribution at the crack-tip region allows K_{II} to take on both positive and negative values. In other words, the crack faces can turn in either downward or upward direction depending on the value of K_{II}. The sequential and weighted sequential models, on the other hand, predict strictly positive values of K_{II}, resulting in a crack-face sliding only in one direction. This is mainly because of the use of effective properties in these simpler multiscale models, which fail to capture local variations in stresses due to particle distribution. The invasive model also predicts strictly positive values of K_{II} due to its failure to capture local stress variations, but also yields a bimodal PDF. This is due to a stronger effect of the explicit presence of material phases at the crack tip. The concurrent models, regardless of κ, again provide excellent estimates of the PDF of K_{II}, including both positive and negative values of K_{II}.

5.2.3. Fracture initiation

The conditional probability of fracture initiation $P_F(K_{Ic}) := P[y(\boldsymbol{R}) < 0]$ of the FGM specimen, where $y(\boldsymbol{R})$ is based on the maximum circumferential theory and defined by Eqs. (12) and (13), was calculated by different multiscale models. Fig. 9 plots how $P_F(K_{Ic})$ varies as a function of the fracture toughness K_{Ic} of the FGM by the multiscale models, including the reference solution from the microscale model. The results indicate that the sequential and weighted sequential models not only fail to capture the effect of material property at the crack tip, but also give misleading information about the failure probability curve. For $P_F(K_{Ic}) < 0.5$, both models significantly underpredict the probability of fracture initiation and are, therefore, unconservative. The invasive

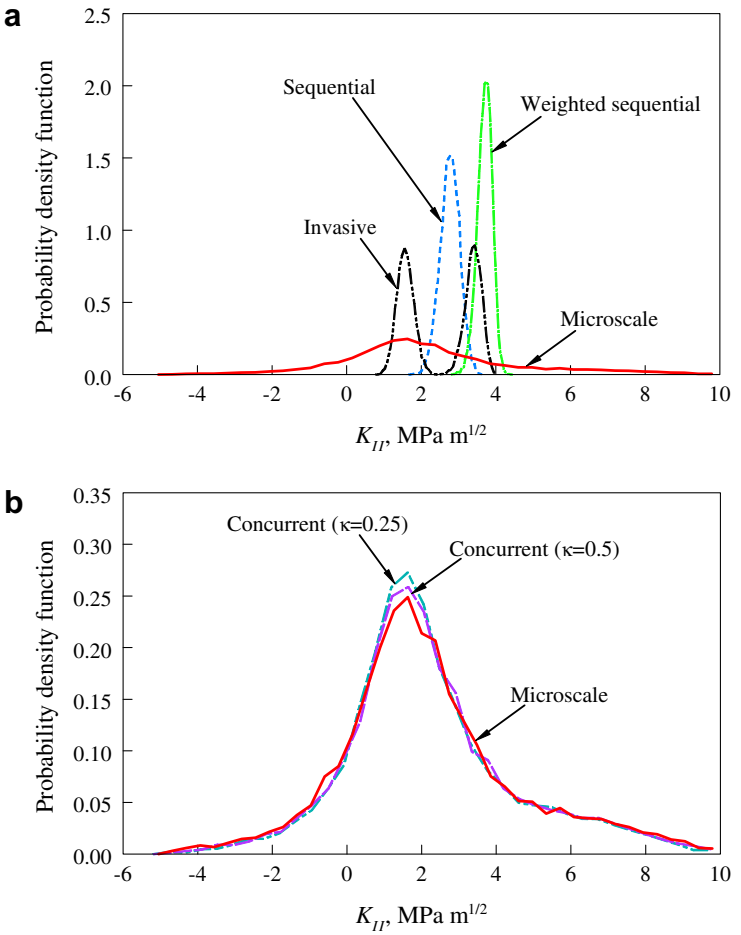

Fig. 8. PDFs of K_{II} by various models: (a) simpler multiscale models; (b) concurrent model.

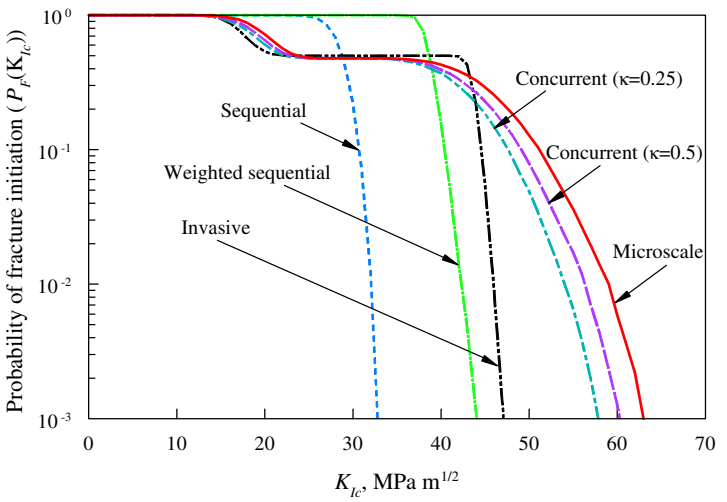

Fig. 9. Probability of fracture initiation by various multiscale and microscale models.

model gives a better estimate of the failure probability curve than those two aforementioned models but still underpredicts failure probabilities less than 0.5. If further accuracy is desired, the concurrent model, which provides more accurate prediction of the probability of fracture initiation than all other multiscale models, can be employed. The accuracy of the concurrent model improves when κ is increased from 0.25 to 0.5, as expected.

5.2.4. Crack propagation

Fig. 10 presents the cumulative distribution function, $P[\Theta < \theta]$, of the initial crack-propagation angle $\Theta(\boldsymbol{R})$ defined by Eq. (13). A comparison of results from different multiscale models indicates once again that the concurrent model provides the best approximation of the distribution function of $\Theta(\boldsymbol{R})$. Since Θ strongly depends on $K_{\mathrm{I}}/K_{\mathrm{II}}$, the sign of K_{II} will have an impact on the direction of crack propagation. Only the concurrent model captures the complete range of Θ comprising positive and negative values, also exhibited by the microscale model.

For simulating crack-propagation, two deterministic samples of the FGM specimen in conjunction with the concurrent model ($\kappa = 0.5$) and the microscale model were examined. The deterministic boundary conditions are the same as before. For both samples, the crack trajectories were determined based on the maximum circumferential stress theory. In addition, the toughness properties of particles and matrix are both lower than crack-driving forces. Fig. 11a shows the crack propagation paths in one sample generated from the concurrent multiscale and microscale models, where the initial propagation direction is downward. For the other sample, where the initial propagation direction is upward, the propagation paths are presented in Fig. 11b, again obtained from both models. It is observed that the concurrent multiscale model ($\kappa = 0.5$) gives almost identical crack propagation paths compared with the microscale model. Further effort should be undertaken to determine if the same conclusion holds for stochastic crack-propagation analysis.

5.3. Further discussion on probabilistic results

The mean results of SIFs listed in Table 2 by all multiscale and microscale models considered in this work are fairly close to each other. For example, the mean values of K_{I} and K_{II}, calculated by the invasive multiscale model, are within 7.2% and 13.5%, respectively, of the microscale model predictions. These differences are not overly large – a finding also reported by Dolbow and Nadeau [11] using their version of the weighted sequential multiscale model. Therefore, one may conclude that simpler multiscale models, such as the invasive model in this work, the weighted sequential model in Dolbow and Nadeau's work [11], and perhaps others, are adequate for calculating crack-driving forces in FGMs. Such conclusion derived from the mean response alone,

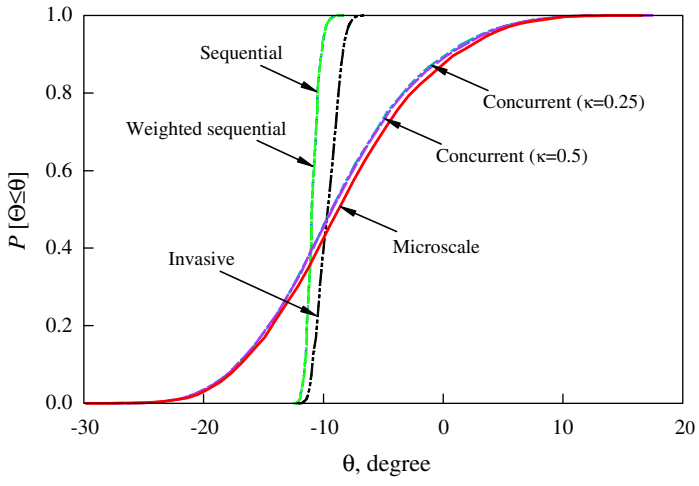

Fig. 10. Cumulative distribution function of initial crack-propagation angle by various multiscale and microscale models.

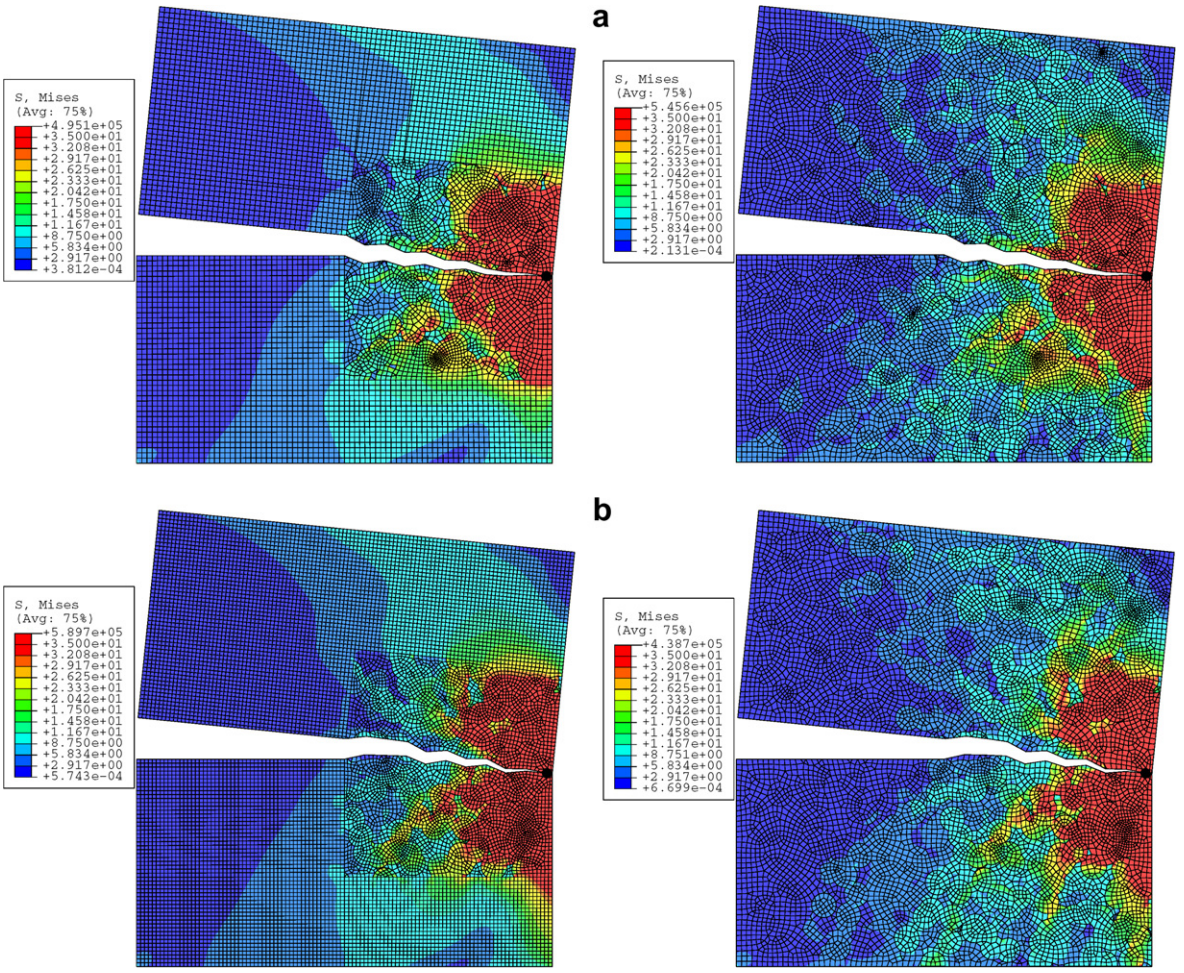

Fig. 11. Simulation of crack propagation: (a) sample 1; (b) sample 2.

which is a common practice in deterministic fracture-mechanics analyses, can be erroneous. For instance, if one examines higher-order moments of fracture response or reliability of FGM, a completely different picture emerges. From Table 2, when comparing the standard deviation (second moment) of SIFs, the predictions from both versions of the sequential model are lower than the microscale solution by an order of magnitude. Therefore, either version of the sequential model is unacceptable. It is interesting to note that the standard deviation of SIF from the invasive model is still accurate, particularly for mode I deformation. When comparing the probability of fracture-initiation curves displayed in Fig. 9, the invasive and sequential model results are lower than those obtained from the microscale or concurrent multiscale model by several orders of magnitude. Therefore, the sequential and invasive models are both unacceptable. The significant discrepancies in results generated from the sequential or invasive model become evident when comparing the tails of the probability distributions. The discrepancy is expected to grow even larger for lower failure probabilities not examined in this work. Therefore, the statistics in Table 2 and, in particular, the probability curves in Fig. 9 are required to determine the accuracy of various multiscale models developed in this work.

The probability curves in Fig. 9 are plotted against any deterministic value of the fracture toughness (K_{Ic}) of FGM. In other words, $P_{\mathrm{F}}(K_{\mathrm{Ic}})$ provides a conditional probability of fracture initiation, given a value of K_{Ic}. In reality, the fracture toughness of an FGM depends on the microstructure (phase volume fraction), varies spatially, and is a random variable or field. In the simplest case, let $K_{Ic,p}$ and $K_{Ic,m}$ represent the deterministic fracture toughness properties of the particle and matrix phases, respectively. Therefore, the unconditional failure probability can be obtained from the weighted average: $\overline{P}_{\mathrm{F}} = P_{\mathrm{F}}(K_{\mathrm{Ic},p})\phi_p(\boldsymbol{x}_{\mathrm{tip}}) + P_{\mathrm{F}}(K_{\mathrm{Ic},m})[1-\phi_p(\boldsymbol{x}_{\mathrm{tip}})]$. If

Table 3
Computational efforts by various models

Model	Relative CPU (single sample)	Relative CPU (full stochastic analysis)
Sequential[a]	0.180	0.020
Weighted sequential[a]	0.180	0.020
Invasive[a]	0.193	0.044
Concurrent ($\kappa = 0.25$)[b]	0.255	0.255
Concurrent ($\kappa = 0.5$)[a]	0.419	0.419
Microscale[a]	1.0	1.0

[a] Using bivariate decomposition method; $N = 12$; $n = 5$; $L = 10{,}000$.
[b] Using direct Monte Carlo simulation; $L = 10{,}000$.

$K_{\mathrm{Ic},p}$ and $K_{\mathrm{Ic},m}$ are random and follow marginal probability densities, $f_p(K_{\mathrm{Ic},p})$ and $f_m(K_{\mathrm{Ic},m})$, of the particle and matrix phases, respectively, the unconditional probability of fracture initiation can then be obtained from the deconditioning: $\overline{P}_{\mathrm{F}} = \int_0^\infty P_{\mathrm{F}}(K_{\mathrm{Ic}}) f(K_{\mathrm{Ic}}) \mathrm{d}K_{\mathrm{Ic}}$, where $f(K_{\mathrm{Ic}}) = f_p(K_{\mathrm{Ic}})\phi_p(\boldsymbol{x}_{\mathrm{tip}}) + f_m(K_{\mathrm{Ic}})[1 - \phi_p(\boldsymbol{x}_{\mathrm{tip}})]$ is the weighted probability density of K_{Ic} of FGM at the crack tip. In either case, the results of Fig. 9 are required and should lead to unconditional fracture-initiation probabilities.

5.4. Computational effort

The fracture analysis involving all multiscale and microscale models were performed in an HP XW4300 workstation. The absolute CPU time required by a single microscale analysis, including all pre-processing efforts, was 120 s. Table 3 lists the relative computational effort by the different multiscale and microscale models examined in this work. The relative CPU time associated with a particular model is defined as the absolute CPU time required by that model divided by the absolute CPU time required by the microscale model. The second column of Table 3 displays the relative CPU time required for a single sample calculation that involves one deterministic finite-element analysis including all pre-processing efforts. The third column of Table 3 describes the relative CPU time for a complete stochastic fracture analysis that leads to the conditional failure probability curve in Fig. 9. For a single sample calculation (second column), the microscale model is the most expensive but also the most accurate. The sequential and weighted sequential models are the most computationally inexpensive models, but they do not produce acceptable results. The invasive model, which gives mixed results, exhibits a similar computational efficiency to that of the previous two multiscale models. The concurrent multiscale model, which produces sufficiently accurate results, is more expensive than other multiscale models but is still less expensive than the microscale model.

For stochastic fracture calculation (third column), the sequential, weighted sequential, and invasive models are substantially more computationally inexpensive than the concurrent multiscale or microscale models. This is due to the lesser CPU time of each deterministic analysis and, more importantly, due to the lower demand of function evaluations in the decomposition method implemented in these multiscale models. Because the concurrent and microscale models employ the direct Monte Carlo simulation with the same sample size, their relative CPU times for a single sample and stochastic analyses remain the same. Nevertheless, the concurrent multiscale model, for either a single sample or stochastic analysis, is always less expensive than the microscale model. For instance, the relative CPU time by the concurrent multiscale model varies from 0.255 to 0.419 when $\kappa = 0.25$ or $\kappa = 0.5$, respectively. Therefore, the computational effort by the microscale model can be reduced by more than half when using a concurrent multiscale model. It is worth noting that the absolute CPU time required by the concurrent model can be further reduced by employing faster simulation methods, such as importance sampling [22] instead of using the direct Monte Carlo simulation. Furthermore, a decomposition method without a reference point, if it can be developed, will also solve the stochastic fracture problem efficiently in terms of computational cost.

6. Conclusions

Three multiscale models, comprising sequential, invasive, and concurrent models, were developed for fracture analysis of a crack in a two-phase, functionally graded composite. The models involve stochastic

description of the particle volume fractions, particle locations, and constituent material properties; a two-scale algorithm including microscale and macroscale analyses for determining crack-driving forces; and two stochastic methods for uncertainty propagation and fracture reliability analysis. The particle volume fractions, defined by a generic inhomogeneous random field, is related to the intensity function of an inhomogeneous Poisson field, which describes the statistically inhomogeneous microstructure of a functionally graded composite. The sequential and invasive multiscale models comprise hierarchically linked microscale and macroscale analyses. The concurrent multiscale model involves simultaneously performed microscale and macroscale analyses. All multiscale models presented were evaluated by the microscale model, which furnishes the reference solutions.

Two stochastic methods, referred to as the dimensional decomposition method and direct Monte Carlo simulation, were applied to obtain the probabilistic characteristics of crack-driving forces and predict the probability of fracture initiation. The dimensional decomposition method involves lower-variate approximations of a crack-driving force, Lagrange interpolations, and Monte Carlo simulation. The decomposition method was used for facilitating a computationally inexpensive stochastic analysis involving either the sequential or invasive multiscale models. However, the stochastic analyses involving the concurrent multiscale and microscale models, so far non-trivially difficult to be handled by the decomposition method, were performed by the direct Monte Carlo simulation.

A numerical example involving an edge-cracked, functionally graded specimen under a mixed-mode deformation was analyzed by the various multiscale and microscale models examined in this work. The results demonstrate that (1) the decomposition methods predict the probability density functions of stress-intensity factors as accurately as direct Monte Carlo simulation but with a significantly lower computational effort; (2) the simpler multiscale models, the sequential, weighted sequential and the invasive models, are the most computationally inexpensive models available, but they do not produce acceptable probabilistic characteristics of stress-intensity factors or accurate probability of fracture initiation; and (3) the concurrent model is sufficiently accurate, gives probabilistic solutions very close to those generated from the microscale model, and can reduce the computational effort of the latter model by more than a factor of two. Finally, a limited yet demonstrative study on crack-propagation simulation indicates that the concurrent multiscale model can predict crack trajectory accurately.

Acknowledgement

The authors would like to acknowledge financial support from the US National Science Foundation under Grant No. CMS-0409463.

References

[1] Suresh S, Mortensen A. Fundamentals of functionally graded materials. London: Institute of Materials; 1998.
[2] Eischen JW. Fracture of nonhomogeneous materials. Int J Fract 1987;34:3–22.
[3] Gu P, Asaro RJ. Cracks in functionally graded materials. Int J Solids Struct 1997;34:1–17.
[4] Jin ZH, Noda N. Crack tip singular fields in nonhomogeneous materials. J Appl Mech 1994;61:738–40.
[5] Rao BN, Rahman S. Meshfree analysis of cracks in isotropic functionally graded materials. Engng Fract Mech 2003;70(1):1–27.
[6] Dolbow JE, Gosz M. On the computation of mixed-mode stress intensity factors in functionally graded materials. Int J Solids Struct 2002;39(9):2557–74.
[7] Kim JH, Paulino GH. Finite element evaluation of mixed-mode stress intensity factors in functionally graded materials. Int J Numer Methods Engng 2002;53(8):1903–35.
[8] Rao BN, Rahman S. An interaction integral method for analysis of cracks in orthotropic functionally graded materials. Comput Mech 2003;32:40–51.
[9] Mura T. Micromechanics of defects in solids. 2nd revised ed. Dordrecht, The Netherlands: Kluwer Academic Publishers; 1991.
[10] Nemat-Nasser S, Hori M. Micromechanics: overall properties of heterogeneous materials. 2nd ed. Amsterdam, The Netherlands: North-Holland; 1999.
[11] Dolbow JE, Nadeau JC. On the use of effective properties for the fracture analysis of microstructured materials. Engng Fract Mech 2002;69:1607–34.
[12] Torquato S. Random heterogeneous materials: microstructures and macroscopic properties. New York, NY: Springer; 2002.
[13] Rahman, S, A random field model for generating synthetic microstructures of functionally graded materials, Int J Numer Methods Engng, submitted for publication.

[14] Ferrante FJ, Graham-Brady LL. Stochastic simulation of non-Gaussian/non-stationary properties in a functionally graded plate. Comput Methods Appl Mech Engng 2005;194:1675–92.
[15] Rahman S, Chakraborty A. A stochastic micromechanical model for elastic properties of functionally graded materials. Mech Mater 2007;39:548–63.
[16] Quintanilla J, Torquato S. Microstructure functions for a model of statistically inhomogeneous random media. Phys Rev E 1997;55(2):1558–65.
[17] Anderson TL. Fracture mechanics–fundamentals and applications. 2nd ed. Boca Raton, Florida: CRC Press; 1995.
[18] Xu H, Rahman S. A generalized dimension-reduction method for multi-dimensional integration in stochastic mechanics. Int J Numer Methods Engng 2004;61:1992–2019.
[19] Xu H, Rahman S. Decomposition methods for structural reliability analysis. Probabilist Engng Mech 2005;20:239–50.
[20] Rubinstein RY. Simulation and the Monte Carlo method. New York, NY: John Wiley and Sons; 1981.
[21] ABAQUS, 2006. User's guide and theoretical manual, Version 6.6, ABAQUS Inc., Providence, RI.
[22] Melchers RE. Importance sampling in structural systems. Struct Safety 1989;6:3–10.